Momentum Fluxes of Gravity Waves Generated by Variable Froude Number Flow Over Three-Dimensional Obstacles

Stephen D. Eckermann *

Space Science Division, Naval Research Laboratory, Washington, DC

John Lindeman

College of Science, George Mason University, Fairfax, VA

Dave Broutman and Jun Ma

Computational Physics, Inc., Springfield, VA, USA

Zafer Boybeyi

College of Science, George Mason University, Fairfax, VA

* *Corresponding author address:* Stephen Eckermann, Code 7646, Space Science Division, Naval Research Laboratory, 4555 Overlook Ave. SW, Washington, DC 20375.

E-mail: stephen.eckermann@nrl.navy.mil

Report Documentation Page

Form Approved
OMB No. 0704-0188

1. REPORT DATE	2. REPORT TYPE	3. DATES COVERED
2010		**00-00-2010 to 00-00-2010**

4. TITLE AND SUBTITLE	5a. CONTRACT NUMBER
Momentum Fluxes of Gravity Waves Generated by Variable Froude Number Flow Over Three-Dimensional Obstacles	5b. GRANT NUMBER
	5c. PROGRAM ELEMENT NUMBER
6. AUTHOR(S)	5d. PROJECT NUMBER
	5e. TASK NUMBER
	5f. WORK UNIT NUMBER
7. PERFORMING ORGANIZATION NAME(S) AND ADDRESS(ES) **Naval Research Laboratory,Space Science Division,Code 7646,Washington,DC,20375**	8. PERFORMING ORGANIZATION REPORT NUMBER
9. SPONSORING/MONITORING AGENCY NAME(S) AND ADDRESS(ES)	10. SPONSOR/MONITOR'S ACRONYM(S)
	11. SPONSOR/MONITOR'S REPORT NUMBER(S)

12. DISTRIBUTION/AVAILABILITY STATEMENT
Approved for public release; distribution unlimited

13. SUPPLEMENTARY NOTES
J. Atmos. Sci. (in press).

14. ABSTRACT
see report

15. SUBJECT TERMS

16. SECURITY CLASSIFICATION OF:			17. LIMITATION OF ABSTRACT	18. NUMBER OF PAGES	19a. NAME OF RESPONSIBLE PERSON
a. REPORT	b. ABSTRACT	c. THIS PAGE			
unclassified	**unclassified**	**unclassified**	**Same as Report (SAR)**	**57**	

ABSTRACT

Fully nonlinear mesoscale model simulations are used to investigate the momentum fluxes of gravity waves that emerge at a "far-field" height of 6 km from steady unsheared flow over both an axisymmetric and elliptical obstacle for nondimensional mountain heights $\hat{h}_m = Fr^{-1}$ in the range 0.1–5, where Fr is the surface Froude number. Fourier- and Hilbert-transform diagnostics of model output yield local estimates of phase-averaged momentum flux, while area integrals of momentum flux quantify the amount of surface pressure drag that translates into far-field gravity waves, referred to here as the "wave drag" component. Estimates of surface and wave drag are compared to parameterization predictions and theory. Surface dynamics transition from linear to high-drag (wave-breaking) states at critical inverse Froude numbers Fr_c^{-1} predicted to within 10% by the transform relations of Smith (1989b). Wave drag peaks at $Fr_c^{-1} < \hat{h}_m \lesssim 2$, where for the elliptical obstacle both surface and wave drag vacillate due to cyclical buildup and breakdown of waves. For the axisymmetric obstacle, this occurs only at $\hat{h}_m = 1.2$. At $\hat{h}_m \gtrsim$2–3 vacillation abates and normalized pressure drag assumes a common normalized form for both obstacles that varies approximately as $\hat{h}_m^{-1.3}$. Wave drag in this range asymptotes to a constant absolute value that, despite its theoretical shortcomings, is predicted to within 10-40% by an analytical relation based on linear clipped-obstacle drag for a Sheppard-based prediction of dividing streamline height. Constant wave drag at $\hat{h}_m \sim$2–5 arises despite large variations with $\hat{h}_m$ in the three-dimensional morphology of the local wave momentum fluxes. Specific implications of these results to the parameterization of subgrid-scale orographic drag in global climate and weather models are discussed.

1. Introduction

Finite computing resources force global numerical weather and climate prediction models to operate at spatial resolutions that prevent an explicit simulation of the full spectrum of dynamics that can arise when surface flow impinges on mesoscale orography. Such dynamics exert drag forces on the larger scale flow and so all credible numerical weather and climate prediction models incorporate parameterizations of these unresolved, or subgrid-scale, orographic mesoscale drag forces (hereafter OMD). Guidance for OMD parameterization comes from observations, numerical modeling and laboratory experiments.

Mesoscale dynamics observed in and around realistic three-dimensional mountain ranges remain challenging to model and reproduce even with state-of-the-art tools (e.g., Smith et al. 2006). More reproducible OMD findings have emerged from idealized numerical and laboratory simulations in which a prescribed upstream flow of constant x–directed velocity U and buoyancy frequency N impinges upon an isolated three-dimensional elliptical obstacle $h(x, y)$ of peak height h_m. A typical form, also used in this work, is

$$h(x, y) = \frac{h_m}{[1 + (x/a)^2 + (y/b)^2]^{3/2}}. \tag{1}$$

To first order, the dynamical response depends on the normalized peak obstacle height

$$\hat{h}_m = N h_m / U = Fr^{-1}, \tag{2}$$

where Fr is surface Froude number. When $\hat{h}_m \ll 1$ flow passes across the obstacle, generating a linear orographic gravity wave response whose three-dimensional form and areally-integrated momentum flux D_L can be computed analytically (Phillips 1984; Smith 1988). As $\hat{h}_m \rightarrow 1$, total pressure drag across the mountain, D_p, begins to exceed the linear solution

D_L by factors of up to ∼2. These so-called "high-drag" states form as flow stagnates aloft (wave breaking) and on the upstream slope (flow splitting), triggering leeside collapse of isentropes, fast downslope winds, turbulence and downstream vortices (Smolarkiewicz and Rotunno 1989; Miranda and James 1992; Ólafsson and Bougeault 1996; Schär and Durran 1997). At $\hat{h}_m \gtrsim$2–3 wave breaking eases or abates and pressure drag eventually drops below D_L. As $\hat{h}_m$ increases, a progressively deeper surface flow layer stagnates upstream and splits, so that only the flow above this layer can pass across the obstacle peak, generating gravity waves of reduced amplitude and wavelength compared to linear predictions (e.g., Ding et al. 2003; Lindeman et al. 2008).

The responses also vary with the obstacle's aspect ratio

$$\beta = b/a. \tag{3}$$

Variations with β in the linear ($\hat{h}_m \ll 1$) hydrostatic limit were derived analytically by Phillips (1984). Dynamical responses close to the mountain as a function of both $\hat{h}_m$ and β were first proposed by Smith (1989b) based on limits of the linear hydrostatic transform relations of Smith (1988) for onset of wave breaking ($\hat{h}_m > \hat{h}_{cb}$) and flow splitting ($\hat{h}_m > \hat{h}_{cs}$).

Figure 1 reproduces the resulting regime diagram, which demarks linear regions at $\hat{h}_m < \hat{h}_c$ in white from various gray-shaded nonlinear responses at $\hat{h}_m > \hat{h}_c$, based on a critical normalized obstacle height (or critical inverse Froude number) $\hat{h}_c = Fr_c^{-1} = \min\left[\hat{h}_{cb}, \hat{h}_{cs}\right]$. At $\beta \gg 1$ it predicts transition from linear wave solutions at $\hat{h}_m \ll 1$ to a wavebreaking-only regime at $\hat{h}_m$ values slightly less than unity, prior to the onset of both wave breaking and flow splitting at $\hat{h}_m \gtrsim 1$. As ellipticity is reduced ($\beta \to 1^+$) the wavebreaking region narrows and eventually disappears at $\beta \sim 1$, due to progressively greater wave-field dispersion. For

$\beta \lesssim 1$ a transition from linear waves to pure flow-splitting dynamics occurs at progressively larger $\hat{h}_c$ values as β decreases, along with progressively smaller pressure drags (Phillips 1984). These predicted regimes have been tested and broadly confirmed using numerical models and tank experiments (e.g., Miranda and James 1992; Ólafsson and Bougeault 1996; Vosper et al. 1999; Bauer et al. 2000; Ding et al. 2003).

Since Figure 1 was formulated by Smith (1989b) for responses in just the lowest few kilometers above the mountain, numerical and laboratory studies have focused on quantifying the total pressure drag across the obstacle and its variation with $\hat{h}_m$ and β and have not quantified the fraction of the pressure drag due to gravity waves that propagate away from the obstacle at larger (nonlinear) $\hat{h}_m$ values. OMD parameterizations require estimates of both the total pressure drag near the mountain and the far-field gravity wave component. Some studies have investigated wave properties and/or momentum fluxes for specific cases (Miranda and James 1992; Vosper et al. 1999; Vosper 2000; Ding et al. 2003; Lindeman et al. 2008; Wells et al. 2008). Yet, despite extensive literature on linear wave properties at $\hat{h}_m \ll 1$ and high-drag wavebreaking states at $\hat{h}_m \sim 1$, we are not aware of any work that has as yet systematically documented both surface pressure drag and gravity wave momentum fluxes from idealized three-dimensional obstacles over the full range of potential $\hat{h}_m$ values: closest perhaps is the work of Welch et al. (2001) for two-dimensional sinusoidal topography (see also Aguilar and Sutherland 2006).

The resulting uncertainty directly impacts the current generation of OMD parameterizations, which have been heavily influenced by this literature on drag due to idealized three-dimensional obstacles. Most modern OMD schemes fit subgridscale mesoscale orography within grid boxes to equivalent elliptical obstacle shapes in order to utilize their documented

drag properties (Lott and Miller 1997; Scinocca and McFarlane 2000), Yet these schemes must quantify both the total surface drag and the propagating gravity-wave component, since gravity waves propagate vertically and can deposit momentum flux at higher altitudes, while the remaining drag is confined and applied near the surface. Given the lack of quantitative guidance on orographic gravity wave momentum fluxes from the modeling literature to date, simple theoretical estimation methods are employed that vary among OMD implementations (Lott and Miller 1997; Gregory et al. 1998; Scinocca and McFarlane 2000; Webster et al. 2003) and require independent research results for objective validation.

Here we conduct fully nonlinear mesoscale model simulations of flow across obstacles of the form (1) at β values of 1 and 3 for a range of $\hat{h}_m$ values shown with solid circles in Figure 1. Our focus is on quantifying the momentum fluxes of propagating gravity waves that emerge at some altitude z_i above the nonlinear surface dynamics near the obstacle, and how these "far field" wave fluxes relate both to the total surface pressure drag and to simpler predictions used in OMD parameterizations.

2. Modeling and Diagnostic Tools

a. WRF Simulations

We use version 3.0 of the Advanced Research WRF (Weather Research and Forecasting) model (Skamarock et al. 2008). The WRF model is nonlinear and fully compressible, discretized with fifth/third-order finite differences for the horizontal/vertical advection, and third-order Runga-Kutta for the time stepping.

Our three-dimensional computational domain, (x, y, z), is square horizontally with the obstacle $h(x, y)$ in (1) located slightly upstream of the domain center to allow more room for dynamics downstream of the obstacle to evolve, such that $-L/3 \leq x \leq 2L/3$ and $-L/2 \leq y \leq L/2$, $L = 900$ km and $z = 0$–30 km. Inflow/outflow conditions are applied at the lateral boundaries. The horizontal gridpoint resolution $(\Delta x, \Delta y)$ is 1.5x1.5 km^2. Our 0–30 km vertical domain is divided into 200 levels using WRF's pressure-based vertical coordinate, 120 of which are below z =15 km where the vertical resolution $\Delta z \approx 125$ m, with Δz gradually increasing above 15 km.

In every experiment we adopt constant vertical profiles of $N = 0.01$ rad s^{-1} and x-directed horizontal velocity $U = +10$ m s^{-1}, then vary h_m and β from experiment to experiment. We choose $a = 10$ km to minimize the rotational and nonhydrostatic linear drag modifications that become significant at larger and smaller widths, respectively (Klemp and Lilly 1980; Miranda and James 1992), then set $b = \beta a$. We adopt a frictionless (free-slip) lower boundary, a 1.5-order turbulent closure scheme, and omit Coriolis effects ($f = 0$) and moisture.

To minimize artificial reflection of gravity waves from the model's rigid lid, the top half of the domain (z = 15–30 km) contains implicit vertically-varying Rayleigh friction of the Klemp et al. (2008) form. Details are given in section 2d.

b. Diagnostic Fourier Transform (FT) Method

To help characterize three-dimensional gravity wave fields in WRF simulations, we employ a diagnostic FT method introduced by Lindeman et al. (2008). The method utilizes the steady state ($t \rightarrow \infty$) form of the time-dependent Fourier-ray algorithm of Broutman

et al. (2006). For the case of vertical velocity

$$w(x,y,z) = \int_{-\infty}^{\infty}\int \tilde{w}(k,l,z)\; e^{\imath(kx+ly)} dk\, dl\;, \tag{4}$$

the method solves for $\tilde{w}(k,l,z)$ using ray methods (Broutman et al. 2002). For the specific case of constant U and N profiles considered here, the Fourier-ray solutions at heights z and z_i are related as

$$\tilde{w}(k,l,z) = \left[\frac{\rho(z_i)}{\rho(z)}\right]^{1/2} \tilde{w}(k,l,z_i) e^{\imath m(z-z_i)}, \tag{5}$$

where vertical wavenumber m follows from the dispersion relation

$$m = -(k^2+l^2)^{1/2}\left(\frac{N^2}{\hat{\omega}^2} - 1\right)^{1/2}, \tag{6}$$

(k,l) is horizontal wavenumber, and, since we assume stationary waves, intrinsic frequency $\hat{\omega} = -kU$. To evaluate (4) we set the Fourier coefficients with $k > 0$ equal to zero (assuming $U > 0$), multiply the Fourier coefficients with $k < 0$ by two, and take the real part of the resulting Fourier transform $\mathring{w}(x,y,z)$, i.e. $w = \mathrm{Re}(\mathring{w})$. The choices of $k < 0$ and $m < 0$ ensure upward (downward) group (phase) propagation. Additional terms in the dispersion relation can be included (Broutman et al. 2009) but are omitted here since they have minor effects. We also omit trapping and tunneling terms (Broutman et al. 2003, 2009) due to the absence of shear.

For linear problems ($\hat{h}_m \ll 1$) the FT method can be initialized at the surface $z_i = 0$ using the orographic elevations $h(x,y)$. The lower boundary condition

$$\tilde{w}(k,l,z_i = 0) = -\imath\hat{\omega}\tilde{h}(k,l), \tag{7}$$

where $\tilde{h}(k,l)$ is the Fourier transform of $h(x,y)$, yields the linear steady-state mountain wave response using (4)-(6).

In characterizing mountain waves in nonlinear WRF simulations ($\hat{h}_m \gtrsim 1$), we assume that nonlinear dynamics are confined to heights $z < z_i$ nearer the mountain, and that a nearly linear stationary steady wave response emerges at z_i after some time t_i (Lindeman et al. 2008). For the case of vertical velocity, WRF output initializes the FT method as

$$\tilde{w}(k, l, z_i) = \tilde{w}_W(k, l, z_i, t_i), \tag{8}$$

where $\tilde{w}_W(k, l, z_i, t_i)$ is the horizontal two-dimensional Fourier transform of the WRF vertical velocity field at height z_i and time t_i. Final values of z_i and t_i are chosen after inspection of the WRF-simulated dynamics (see section 2d): typical values used in our work will be $z_i = 6$ km and $t_i = 24$ hours.

The gravity-wave polarization relations allow us to convert $\tilde{w}(k, l, z)$ into corresponding solutions for other variables, such as the horizontal velocity components $\tilde{u}$ and $\tilde{v}$. Here we utilize the resulting complex spatial solutions $\mathring{u}$, $\mathring{v}$, and $\mathring{w}$, defined earlier, whose real parts are the FT solution (4) for $\tilde{u}$, $\tilde{v}$ and $\tilde{w}$, respectively, and whose imaginary parts are the Hilbert transforms of those FT solutions, thus providing local amplitudes and phases of the velocity solutions (e.g., Mercier et al. 2008). This latter property, together with the $n\pi$ phase difference between horizontal and vertical velocity components ($n \in \mathbf{Z}$), allow us to combine $\mathring{u}$, $\mathring{v}$, and $\mathring{w}$ to yield local solutions of phase-averaged momentum flux per unit mass

$$\overline{uw}(x, y, z) = \frac{1}{4}\left(\mathring{u}\mathring{w}^* + \mathring{u}^*\mathring{w}\right), \tag{9}$$

$$\overline{vw}(x, y, z) = \frac{1}{4}\left(\mathring{v}\mathring{w}^* + \mathring{v}^*\mathring{w}\right). \tag{10}$$

where asterisks denote a complex conjugate. The relations (9) and (10) differ from other local diagnostics used to quantify wave momentum fluxes (e.g., Durran 1995) by using a

Fourier-ray decomposition of the WRF output to synthesize a phase-averaged result. Their fidelity depends on the linear stationary wave assumptions underpinning this FT method, and so are assessed when applied to WRF output in what follows.

c. Drag

1) Surface Pressure Drag

The total surface pressure drag across the obstacle

$$\mathbf{D_p} = \int_{-\infty}^{\infty}\int p' \left(\frac{\partial h}{\partial x}, \frac{\partial h}{\partial y}\right) dx\, dy, \tag{11}$$

where p' is the surface pressure anomaly (hereafter we denote WRF anomalies with lowercase primed symbols to distinguish them from spatial realizations of the Fourier-ray solutions which are unprimed lowercase).

In the linear ($\hat{h}_m \ll 1$) hydrostatic approximation, (1) and (11) yield analytical drag solutions of the form

$$|\mathbf{D_L}| = D_L(\beta) = B(\beta) a \rho_0 N U h_m^2, \tag{12}$$

where ρ_0 is upstream surface density, and $B(\beta)$ is the scaling form factor for the obstacle (1) (Phillips 1984). In our WRF runs, U and N remain constant while peak mountain heights h_m are varied. Thus, the linear drag (12) scales with $\hat{h}_m = Fr^{-1}$ in our WRF runs as

$$|\mathbf{D_L}| = B(\beta) a \rho_0 \frac{U^3}{N} \hat{h}_m^2, \tag{13}$$

and peaks at the largest (nonlinear) $\hat{h}_m$ values.

Consistent with previous studies (e.g., Miranda and James 1992; Bauer et al. 2000), it will prove most useful for parameterization applications to study nondimensional drag values

normalized by the relevant linear prediction: e.g.

$$\hat{D}_p = \frac{D_p}{D_L}. \tag{14}$$

In computing $D_p = |\mathbf{D_p}|$, since U is x-directed, only the x-component of $\mathbf{D_p}$ strictly acts a drag on the flow and, due to the symmetry of the problem, the y components (sometimes referred to as lift forces) should integrate to zero. Accordingly many studies simply compute the x-component of (11) only (e.g., Epifanio and Durran 2001). For consistency, here we compute both components and evaluate (11) by integrating over the full horizontal WRF domain of $-L/3 \leq x \leq 2L/3$ and $-L/2 \leq y \leq L/2$.

2) Gravity-Wave Contribution: "Wave Drag"

The component of the drag due to propagating gravity waves at a given height z is

$$\mathbf{D_w}(z) = \rho(z) \int_{-L/3}^{+2L/3} \int_{-L/2}^{+L/2} (u'w', v'w')\, dx\, dy, \tag{15}$$

where u', v' and w' are local WRF zonal, meridional and vertical velocity anomalies, respectively, at height z. In the linear regime one should recover $D_w(z) = D_p \approx D_L$ at all heights, a property we utilize in section 2d to tune the WRF sponge layer.

The FT method yields corresponding terms

$$\mathbf{D_{f_1}}(z) = \rho(z) \int_{-L/3}^{+2L/3} \int_{-L/2}^{+L/2} (uw, vw)\, dx\, dy, \tag{16}$$

$$\mathbf{D_{f_2}}(z) = \rho(z) \int_{-L/3}^{+2L/3} \int_{-L/2}^{+L/2} (\overline{uw}, \overline{vw})\, dx\, dy. \tag{17}$$

The first expression is the FT analogue of the WRF expression (15) using individual Fourier-ray solutions for u, v and w. The second expression integrates the phase-averaged Fourier-ray

covariance solutions (9) and (10). Since (16) and (17) give identical results, for simplicity here we only use D_{f_2} and refer to it as the diagnostic Fourier-ray drag D_f. We also compute a linear FT drag D_{fL} computed from (17) using the linear boundary condition (7).

Since these expressions, along with (11), quantify the fraction of the surface pressure drag D_p that appears at some height z as gravity-wave momentum flux, we will refer to them as "wave drag" estimates. This is not to be confused with the wave drag considered in OMD parameterizations, which is the decelerative force on the atmosphere due to dissipation of orographic gravity-wave momentum flux with altitude, which we do not study in this paper.

d. Tuning and Validation

A series of linear ($\hat{h}_m \ll 1$) WRF experiments were performed with varying sponge layer depths and damping rates until computed drag D_w reproduced the $t \to \infty$ linear prediction D_L after time t_i without subsidiary structure due to partial reflections. We settled upon a vertical damping profile from z =15–30 km based on eq. (21) of Klemp et al. (2008) with a damping coefficient at $z = 30$ km of 0.2 s^{-1}, slightly larger than the value chosen by Klemp et al. (2008) due to our deeper sponge layer and higher horizontal resolution.

Figure 2a plots resulting $\hat{D}_w = D_w/D_L$ profiles at 6 hourly intervals for a $\beta = 1$, $\hat{h}_m = 0.1$ obstacle. The profile equilibrates after ∼18 hours to values close to the hydrostatic linear solution $\hat{D}_L = 1$ with little evidence of spurious structure due to sponge-layer reflections. Figure 2b plots the corresponding time series of (normalized) wave drag $\hat{D}_w$ and $\hat{D}_f$ at $z_i = 6$ km, along with surface pressure drag $\hat{D}_p$ and the linear $t \to \infty$ predictions $\hat{D}_L$ and

$\hat{D}_{fL}$. While surface drag $\hat{D}_p \rightarrow \hat{D}_L = 1$ in Figure 2b after only a few hours, wave drag $\hat{D}_w$ builds up over time to a limiting value of ~ 0.975 after $\sim$20 hours, showing that $t_i = 24$ hours is long enough to generate the equilibrium wave response at $z_i = 6$ km.

This $\sim$2% reduction in D_w from D_L in Figure 2b was also noted by Schär and Durran (1997) in their $\hat{h}_m$ =0.05 simulation for an axisymmetric $a = 10$ km obstacle. About half of this difference is explained by the $\sim$1% difference between the linear Fourier-ray drag D_{fL} and D_L due to a small nonhydrostatic reduction in drag in the former due to evanescent modes. The remaining difference is due to lateral propagation of wave flux through the WRF side boundaries, which D_{fL} does not suffer from due to periodic boundary conditions and wraparound. This boundary absorption increases with altitude as wave fields propagate upwards and disperse more horizontally, as evident in the $\hat{D}_w$ profiles in Figure 2a.

Note too that the $\hat{D}_f$ and $\hat{D}_w$ curves in Figure 2b lie virtually on top of one another, confirming the fidelity of the diagnostic FT relations presented in section 2b for this linear example. Detailed validation of these FT flux diagnostics for other linear cases simulated with WRF can be found in Lindeman (2008).

3. Drag Evolution for the Axisymmetric Obstacle

Figure 3 plots the time evolution of the drag due to the axisymmetric obstacle ($\beta = 1$) as $\hat{h}_m$ is progressively increased from 0.1 to 1.5. The drag values are normalized by the linear hydrostatic prediction (12), where $B(1) = \pi/4$ (Phillips 1984).

As $\hat{h}_m \rightarrow 1^-$, the equilibrium surface pressure drag $\hat{D}_p$ becomes progressively larger than unity ($\hat{D}_L$). In the $\hat{h}_m$ =0.1–1.0 range no turbulent kinetic energy (TKE) is generated and

essentially all the surface drag translates into propagating gravity wave momentum flux at $z_i = 6$ km ($\hat{D}_w \approx \hat{D}_p$), consistent with the predictions of Figure 1. However, Figure 1 also shows that $\hat{h}_m$ values slightly larger than unity enter a junction point where all the dynamical regimes meet and no clear dynamical response is predicted.

A small increase in $\hat{h}_m$ from 1.0 to 1.2 triggers an abrupt change in simulated drag behavior in Figure 3g. Surface drag $\hat{D}_p$ becomes ∼50% larger than linear predictions and equilibrates to an oscillating state with a period of close to 4 hours. Wave drag $\hat{D}_w$ and $\hat{D}_f$ at $z_i = 6$ km track one another well and show similar 4-hour cycling seen in $\hat{D}_p$, but typically at 15–20% lower values and with a slight phase lag due to vertical propagation. Thus surface drag no longer translates fully into a propagating wave response at 6 km altitude.

The periodic nature of the drag is due to cyclical wave buildup and breakdown, as depicted in Figure 4 for the cycle between hours 20 and 24. At hour 20, D_p is large while D_w is reduced (Figure 3g) as forced waves propagate upwards and build in amplitude at $z_i = 6$ km. One hour later wave drag D_w has grown to the point where isentropes at $z \sim 3$ km in Figure 4b are superadiabatic and generating enhanced TKE. At hour 22 wave breaking peaks with a large burst of TKE descending the obstacle downslope. This TKE has migrated downstream by hour 23, at which time both surface drag and wave drag have been reduced by accumulated local turbulent dissipation and/or upstream responses to wave breaking that increase flow splitting. At hour 24 the isentropic and TKE structures in Figure 4e return to a morphology almost identical to that at hour 20 as surface drag and wave activity build up again and the cycle repeats. Note that TKE (strong nonlinearity) is confined below z_i =6 km, consistent with requirements of the FT method and with the agreement between $\hat{D}_w$ and $\hat{D}_f$ in Figure 3e. Despite much shorter time series, axisymmetric obstacle simulations of

Miranda and James (1992) and Vosper (2000) show evidence of similar periodic vacillations in both surface and wave drag, but at larger $\hat{h}_m$ values.

A further increase of $\hat{h}_m$ to 1.5 yields a high-drag state with wave breaking above the lee downslope. In contrast to our $\hat{h}_m = 1.2$ result and the $\hat{h}_m = 1.5$ results of Miranda and James (1992), however, drag in Figure 3h does not vacillate periodically. $\hat{D}_p$ instead settles to an approximate equilibrium value of $\sim$1.3 while $\hat{D}_w$ builds up gradually to an equilibrium value of $\sim$0.9. The former compares favorably to the nonvacillating equilibrium $\hat{D}_p$ $\sim$1.2 found by Schär and Durran (1997).

Figure 5 plots local gravity-wave momentum fluxes at z_i =6 km after 24 hours, as derived from WRF output using the FT relations (9) and (10). Figure 5a reveals the expected linear ship-wave response (Smith 1980) at $\hat{h}_m = 0.1$, with net westward $\rho\overline{uw}(x, y, z)$ peaking in magnitude near the obstacle peak, and smaller $\rho\overline{vw}(x, y, z)$ values distributed antisymmetrically about y =0 and peaking in magnitude in the divergent wing regions. While wave fluxes at $\hat{h} = 1.0$ in Figure 5b are two orders of magnitude larger [consistent with the scaling (13)], the wave pattern is very similar, except the region of maximum $\rho|\overline{uw}|$ is now displaced slightly downstream. At $\hat{h}_m = 1.2$ and 1.5, wave momentum flux patterns are noticeably modified. Peak $|\rho\overline{uw}|$ regions are narrower and located above the obstacle downslope. For $\hat{h}_m = 1.5$, Lindeman et al. (2008) showed that this results from leeside collapse and ascent of isentropes, which provide a sharp deep region of obstacle-like forcing to the flow that controls the form of the waves at 6 km more than the actual obstacle shape (see also Figure 4). This narrower forcing generates waves with shorter horizontal wavelengths (Ding et al. 2003; Lindeman et al. 2008), and it's less axisymmetric nature reduces three-dimensional propagation of momentum flux into diverging wing regions in Figures 5c and 5d.

Figure 6 plots the drag time series for $\hat{h}_m$ =2–5. Similar responses are seen in all cases. $\hat{D}_p$ decreases with time to values below unity and does not equilibrate after 24 hours. By contrast, $\hat{D}_w$ steadily increases with time and equilibrates after ∼15 hours at values significantly smaller than $\hat{D}_p$, consistent with greater flow splitting and lee-vortex generation at these larger $\hat{h}_m$ values (Schär and Durran 1997).

A cross section of isentropes and TKE at $y = 0$ after 24 hours is shown in Figure 7 for the $\hat{h}_m = 3$ simulation. A sharp zone of isentropic collapse and ascent is evident above the top third of the lee downslope, with TKE peaked sharply within this leeside trough at unstable temperature gradients. As for the $\hat{h}_m$ =1.5 obstacle (Lindeman et al. 2008), Figure 7 shows that this leeside isentropic structure provides the major obstacle-like forcing for the waves that emerge at $z_i = 6$ km, which are concentrated downstream of the obstacle peak. Similar leeside offsets in wave activity are evident in the $\hat{h}_m = 3.0$ results of Schär and Durran (1997). Since the leeside isentropic structure in Figure 7 is quite steady with time (not shown), the wave fields it forces are approximately stationary and steady, and thus their integrated momentum fluxes $\hat{D}_w$ are well described by the FT diagnostic $\hat{D}_f$ in Figure 6b.

Figure 8 shows the corresponding local wave momentum fluxes $\rho\overline{uw}$ and $\rho\overline{vw}$ at 6 km. Zonal fluxes peak in magnitude above the obstacle downslope due to stationary obstacle-like forcing by lee-side isentropic structures as in Figure 7. These peak fluxes are concentrated within regions of progressively smaller horizontal extent as $\hat{h}_m$ increases, consistent with a progressively higher dividing streamline and flow above passing over a smaller narrower uppermost obstacle peak, forcing waves of correspondingly smaller horizontal wavelength (see Figure 7). At the largest (most nonlinear) $\hat{h}_m = 4$ and 5, subsidiary $|\rho\overline{uw}|$ maxima appear in Figure 8c and 8d at the lateral edges of the obstacle, due to flow splitting and diversion

around the obstacle peak, resulting in Bernoulli-type accelerations that force waves at the cross-stream extremities of the obstacle. A similar high–$\hat{h}_m$ transition in wave forcing to the outer edges of the obstacle was seen in the $\beta = 5$ simulations of Ólafsson and Bougeault (1996). The fine-scale wave structures at the largest $\hat{h}_m$ may be compromised somewhat by our 1.5 km gridpoint resolution as the clipped obstacle width for wave forcing becomes progressively narrower as the dividing streamline gets progressively higher with increasing $\hat{h}_m$.

Since some drag responses do not obviously equilibrate after 24 hours, the $\hat{h}_m = 1.2$ and 3.0 WRF simulations were integrated out to 48 hours. Figure 9 shows the resulting drag profiles. Oscillatory pressure and wave drag at $\hat{h}_m = 1.2$ is clearly a robust equilibrium result. The secular decrease in $\hat{D}_p$ out to 24 hours seen for $\hat{h}_m = 3.0$ abates in Figure 9b after ∼28 hours, wherepon $\hat{D}_p$ increases slightly then equilibrates at ∼0.5 at ∼36 hours. Wave fluxes remain largely unchanged during this period. These integrations suggest that drag in the 20-24 hour range is close to the long-time-limit equilibrium response.

Thus Figure 10 plots mean drag as a function of $\hat{h}_m$ over the 20–24 hour equilibrium range, both in normalized and absolute form. At $0 < \hat{h}_m < 1$, Figure 10a shows a gradual linear increase in $\hat{D}_p$ above unity. A similar small linear increase over this $\hat{h}_m$ range was modeled by Epifanio and Durran (2001) using weakly-nonlinear semianalytical theory. This linear trend breaks at $\hat{h}_m \gtrsim 1$ with the onset of a peak oscillating high-drag wavebreaking state of $\hat{D}_p$ =1.4-1.55 at $\hat{h}_m = 1.2$, with $\hat{D}_p$ decreasing monotonically with $\hat{h}_m$ thereafter. This mean $\hat{D}_p$ variation with $\hat{h}_m$ agrees with that found by Bauer et al. (2000) (who used a slightly different obstacle shape) but differs somewhat from the results of Miranda and James (1992), who found $\hat{D}_p$ peaking at ∼1.8 at $\hat{h}_m \sim 1.5$. Our $\hat{D}_p$ values at $\hat{h}_m$ =1.5

and 3 are similar to those of Schär and Durran (1997) but are again smaller than those of Miranda and James (1992). Our results support the contention of Bauer et al. (2000) that the Miranda and James (1992) drag values are systematically too large.

Next we study mean D_w values and how they relate to surface pressure drag in the nonlinear $\hat{h}_m$ range where $D_w/D_p < 1$. A common parameterization approach is to estimate the height z_{ds} of the dividing streamline, separating flow over the obstacle peak ($z > z_{ds}$) from flow blocked or diverted around the obstacle ($z < z_{ds}$), as

$$z_{ds} = (1 - \alpha Fr)\, h_m = \left(h_m - \alpha \frac{U}{N} \right) \tag{18}$$

(Hunt and Snyder 1980), where

$$\alpha \equiv \hat{h}_{cs} = Fr_{cs}^{-1}, \tag{19}$$

the critical inverse Froude number for flow splitting. The "clipped" obstacle for wave forcing is then $h_c(x, y) = \max[h(x, y), z_{ds}]$ (Lindeman et al. 2008) which has a peak height

$$(h_c)_m = h_m - z_{ds} = \alpha \frac{U}{N}, \tag{20}$$

whose normalized height, from (2), is equal to α. Figure 1 predicts that α varies with β, and it can also vary with different definitions of z_{ds} (see section 6.6 of Baines 1995). Here, for simplicity, we will adopt the Sheppard criterion of $\alpha = 1$ which, despite its theoretical shortcomings (Smith 1989b), reproduces laboratory measurements of z_{ds} (Snyder et al. 1985; Vosper et al. 1999; Ding et al. 2003).

Large triangles in Figure 10a show the resulting wave drag $\hat{D}_c$ calculated by the FT method using $h_c(x, y)$ as the linear boundary condition (7) at $z_i = z_{ds}$. An even simpler analytical approximation assumes the linear solution (12) for the clipped obstacle height

$(h_c)_m$, which yields a constant "saturated" clipped wave drag (see Appendix A) of

$$D_{c1} = B(\beta) a \rho_0 \alpha^2 \frac{U^3}{N}, \tag{21}$$

plotted with small triangles in Figure 10b.

Both D_c and D_{c1} systematically underestimate the actual wave drag at $\hat{h}_m \gtrsim 1$ in Figure 10. Nonetheless, D_{c1} reproduces the flat trend in D_w at $\hat{h}_m > 2.5$ in Figure 10b but with $D_w/D_{c1} \approx 1.5$: an α of 1.2 instead of 1 would make this ratio near unity, a choice that can be justified from Figures 1, 3 and 10a. D_w/D_{c1} is larger in the range $\hat{h}_m$ =1.2–2 with a peak near 2, demarking this region as a "high wave-drag state."

It is also useful to study how D_w might scale with D_p given that many OMD parameterizations quantify gravity-wave fluxes by scaling surface drag. A reasonable D_p-scaled empirical fit to D_w at all $\hat{h}_m$, shown as the solid gray curve in Figure 10, is:

$$D_w \approx D_{fit} = \begin{cases} D_p & 0 \le \hat{h}_m \le 1, \\ D_p \hat{h}_m^{-0.9} & 1 < \hat{h}_m \le 2.5, \\ (D_p \hat{h}_m^{-0.9})|_{\hat{h}_m = 2.5} & \hat{h}_m > 2.5. \end{cases} \tag{22}$$

4. Drag Evolution for the Elliptical Obstacle

Figure 11 plots time evolution of the elliptical ($\beta = 3$) obstacle drag as $\hat{h}_m$ is increased from 0.1 to 1.5. Again, drag is normalized by the corresponding hydrostatic linear prediction D_L in (12), where $B(3) \approx 0.9369\beta \approx 2.82$ (Phillips 1984). Thus the linear drag in this case is enhanced over that of the axisymmetric obstacle by $D_L(3)/D_L(1) = B(3)/B(1) \approx 3.6$.

At $\beta = 3$, Figure 1 predicts nonbreaking waves at $0 < \hat{h}_m < \hat{h}_{cb} \sim 0.73$, followed by an extended wave breaking regime at $\hat{h}_m > \hat{h}_{cb}$. Drag at $\hat{h}_m$ =0.1–0.5 in Figure 11 reveals pure

wave responses, for which $\hat{D}_p \approx \hat{D}_w \approx \hat{D}_f \approx D_L$, that generate no TKE. The $\hat{h}_m = 0.7$ drag in Figure 11d oscillates due to small vacillating levels of TKE (peaking at ∼0.01–0.05 $\mathrm{m^2\ s^{-2}}$) that form at unstable wave phases, consistent with the predicted wave breaking threshold of $\hat{h}_{cb} \sim 0.73$ in Figure 1. At $\hat{h}_m$ =0.85–1.5, strong wave breaking dynamics are simulated, again consistent with Figure 1. The surface drag $\hat{D}_p$ at $\hat{h}_m$ =0.85–1.5 undergoes large cyclical excursions with a period that decreases from ∼9 hours at $\hat{h}_m = 0.85$ (Figure 11e) to ∼6 hours at $\hat{h}_m = 1.5$ (Figure 11h).

Unlike the corresponding $\beta = 1$ results in Figure 3, the diagnostic FT wave drag $\hat{D}_f$ does not reproduce $\hat{D}_w$ well at $\hat{h}_m \gtrsim 0.7$ in Figure 11. Reasons why are highlighted in Figure 12, which plots isentropes and TKE cross sections at 2 hourly intervals along the $y = 0$ axis for the $\hat{h}_m = 0.85$ simulation. At hour 3 when D_f and D_w agree in Figure 11e, nonlinearity in the form of overturning isentropes and large levels of TKE is confined below $z_i = 6$ km (where $\hat{D}_f$ and $\hat{D}_w$ are evaluated), consistent with the assumptions of the FT method (see section 2b). However, unlike the $\beta = 1$ cases (see Figure 4), nonlinearity is not confined below 6 km at later times. For example, at hour 7 there is strong overturning and turbulent mixing at ∼10 km altitude (Figure 12c). At later times high-altitude wave activity is evident well downstream of the obstacle in Figures 12d and 12e. The sources of these waves are near-surface wake dynamics (e.g., Dupont et al. 2001) and wavebreaking regions at higher altitudes (e.g., Bacmeister and Schoeberl 1989; Satomura and Sato 1999; Tan and Eckermann 2000). The resulting waves are generally nonstationary and some may propagate downwards (Bacmeister and Schoeberl 1989), and thus are not properly characterized by the stationary upgoing gravity-wave dispersion relation (6) that underpins the FT diagnostics.

Drag at the larger $\hat{h}_m$ values of 2–5 is plotted in Figure 13. The vacillating wave breaking

regime extends to at least $\hat{h}_m = 3$, where the drag vacillation is now weak and its period has reduced to ∼4 hours (Figure 13b). At still larger $\hat{h}_m$ the pressure drag decreases more uniformly with time and wave drag settles to equilibrium values, similar to the behavior found for the $\beta = 1$ obstacle at similarly large $\hat{h}_m$ values in Figure 6.

Given the large drag vacillations for the $\beta = 3$ obstacle, mean drag is computed over the last 12 hours of each simulation, with resulting means and standard deviations plotted in Figure 14. Mean drag in the range $0 < \hat{h}_m \lesssim 0.5$ does not exhibit a noticeable linear increase with $\hat{h}_m$ as was found for the axisymmetric obstacle, but instead tracks the hydrostatic analytical value of $\hat{D}_L = 1$ closely. This persists to $\hat{h}_m = 0.7$ despite the vacillation in Figure 11d and associated standard deviation in Figure 14. At $\hat{h}_m = 0.85$, a large abrupt increase occurs in both $\hat{D}_p$ and its standard deviation, due to sudden onset of a vacillating high-drag wavebreaking state. The high-drag $\hat{D}_p$ enhancements peak at $\hat{h}_m \sim 1$. At larger $\hat{h}_m$, mean $\hat{D}_p$ decreases monotonically as do the associated standard deviations. Wells et al. (2008) report a mean $\hat{D}_p \sim 1.1$ at $\hat{h}_m = 2$ in their Boussinesq simulations without Coriolis terms, somewhat larger than our mean value here of 0.83 ± 0.13.

Wave drag $\hat{D}_w$, which tracks $\hat{D}_p$ and $\hat{D}_L$ at small $\hat{h}_m$, drops abruptly below $\hat{D}_p$ at $\hat{h}_m \gtrsim 0.85$ as wave breaking and (at larger $\hat{h}_m$) flow splitting cause progressively greater fractions of the surface pressure drag to manifest as near-surface dynamics rather than gravity waves. Despite the strongly nonlinear dynamics that yield a generally nonstationary nonlinear wave field at $z_i = 6$ km (Figure 12), the unnormalized areally-averaged momentum flux D_w is fitted fairly well throughout the extended nonlinear range $\hat{h}_m \approx 0.85$–5 in Figure 14b by the simple clipped obstacle prediction $\hat{D}_{c1}$ in (21). For example, mean D_w values at $\hat{h}_m$ =3–5 are only ∼10–20% larger than D_{c1}. At $\hat{h}_m$ =0.85–3, D_w exceeds D_{c1} by more than this factor,

consistent with this range of $\hat{h}_m$ being a high-drag wave-breaking state.

5. Discussion

Figure 15 compares the mean normalized surface-pressure and far-field wave drags for the $\beta = 1$ and $\beta = 3$ obstacles as a function of $\hat{h}_m$. While $\hat{D}_w = \hat{D}_p$ for both obstacles in the mutual "linear" (non-TKE) range $\hat{h}_m$ ∼0.1–0.7, the $\hat{D}_w$ curve for the axisymmetric obstacle increases linearly with $\hat{h}_m$ in this range to values progressively larger than unity, whereas the $\hat{D}_w$ curve for the elliptical $\beta = 3$ obstacle stays close to the hydrostatic linear prediction of $\hat{D}_L = 1$.

In the high-drag region of $\hat{h}_m$ ∼1–2, mean $\hat{D}_p$ values for the $\beta = 3$ obstacle peak at a smaller $\hat{h}_m$ and attain larger values than for the axisymmetric obstacle, and individual values exhibit a much larger variation with time (standard deviation). This is broadly consistent both with Figure 1 and the more intense wave breaking (relative to axisymmetric obstacles) expected for elliptical obstacles (1) whose long axis b is aligned perpendicular to the flow, due to less dispersion of wave activity that leads to more concentrated and unstable wave fields. The smaller D_w values at $z_i = 6$ km for the $\beta = 3$ compared to $\beta = 1$ obstacle are consistent with greater near-surface dissipation of waves by overturning and TKE in the $\beta = 3$ simulations (c.f. Figures 4 and 12).

In the nominal flow-splitting regime of $\hat{h}_m \gtrsim 2$, $\hat{D}_p$ values in Figure 15 are almost identical for both obstacles. Using a different obstacle shape, Bauer et al. (2000) also found very similar $\hat{D}_p$ values at large $\hat{h}_m$ for β =1–4. Some analytical models of flow-blocking drag predict $\hat{D}_p \propto \hat{h}_m^{-1}$ at large $\hat{h}_m$ (Lott and Miller 1997; Scinocca and McFarlane 2000), while

others suggest $\hat{D}_p \approx \hat{D}_L \sim 1$ due to surface drag enhancements from rotation and friction (Webster et al. 2003). Our common $\hat{D}_p$ curve is well fit as $\hat{h}_m^{-1.3}$ at $\hat{h}_m$ =2–5. Stein (1992) reported a $\hat{D}_p$ fit $\propto \hat{h}_m^{-0.7}$ in this range based on two-dimensional simulations.

Absolute wave drag D_w at $\hat{h}_m$ ∼2.5–5 was almost constant for both the $\beta = 1$ and $\beta = 3$ obstacles, and predicted reasonably accurately by scaling the "saturated" linear wave drag D_{c1} given by (21) (see Figures 10b and 14b). It is remarkable that D_w values are all so similar in this range, given the large variation in local wave momentum-flux morphology as a function of $\hat{h}_m$ in Figure 8, and nonstationary transient waves from surface wake and TKE sources for the $\beta = 3$ obstacle in Figure 12. While this $D_w \sim D_{c1}$ finding may prove to be very convenient for parameterizing orographic gravity wave momentum fluxes in this range, it must be recognized that the simple theoretical arguments that yield D_{c1} (see Appendix A) are inconsistent with the WRF-simulated wave fields. As explicitly demonstrated by Lindeman et al. (2008), the effective obstacle forcing for these waves does not resemble the clipped obstacle forcing underpinning D_{c1}. It is instead dominated by obstacle-like forcing produced by the leeside fluid dynamical response, specifically the sharp descent and ascent of isentropes along the obstacle downslope (see Figure 7), which yield highly concentrated wave momentum flux in Figure 8 above the obstacle downslope, rather than near the peak. In short, (21) gives an approximately correct answer but for demonstrably wrong reasons. Why D_{c1} is a reasonable fit to modeled wave fluxes in this nonlinear range is not yet clear, but this need not be a barrier to using it in parameterizations. For example, parameterizations based the saturated gravity-wave spectra observed in the middle atmosphere are now common in models, despite the lack of an accepted theory for how these spectra are formed (McLandress and Scinocca 2005).

Indeed, several OMD parameterizations already use relations akin to D_{c1} to assign wave momentum fluxes in this nonlinear h_m range (Scinocca and McFarlane 2000; Webster et al. 2003). The value of α, defined equivalently in these OMD schemes via (19) as the critical inverse Froude number Fr_c^{-1} (since $Fr_{cb}^{-1} \approx Fr_{cs}^{-1}$ is also assumed), must be chosen. Originally these schemes used Fr_c^{-1} ~0.5–1 (Scinocca and McFarlane 2000; Webster et al. 2003) but, given a lack of theoretical closure on D_w/D_p values at $\hat{h}_m \geq Fr_c^{-1}$, Fr_c^{-1} has been used as a "free" tuning parameter in models and subsequently revised downwards to ~0.25–0.375 to improve skill (Wells et al. 2005; Scinocca et al. 2008). Given our finding of D_w/D_{c1} ~1.1–2.0 for a D_{c1} calculation using $Fr_{cs}^{-1} = \alpha = 1$ and the Fr_{cs}^{-2} dependence of D_{c1} in (21), these results imply order of magnitude underestimates of orographic gravity wave momentum fluxes at $\hat{h}_m \gtrsim 1$ for Fr_c ~0.25–0.375.

This is illustrated further in Figure 16, which plots D_w/D_p as a function of $\hat{h}_m$ for both the $\beta = 1$ and $\beta = 3$ obstacles. Some previous simulations have suggested that D_w/D_p rapidly decreases at $\hat{h}_m \gtrsim Fr_c^{-1}$ and essentially vanishes at large $\hat{h}_m$ (Miranda and James 1992; Wells et al. 2005). While D_w/D_p certainly drops suddenly below unity at $\hat{h}_m \sim Fr_c^{-1}$ in Figure 16, especially for the $\beta = 3$ obstacle, our results also show that, even at large $\hat{h}_m$ ~2–5, propagating "far field" gravity waves remain a significant (>20%) fraction of the total pressure drag. Our $\hat{h}_m = 2$, $\beta = 3$ value of 0.43 ± 0.10 at $z_i = 6$ km in Figure 16b compares reasonably to a corresponding value of ~0.52 evaluated by Wells et al. (2008) at ~100 m above their obstacle peak. The slightly smaller mean value here is consistent with some additional near-field turbulent dissipation of waves in propagating to $z_i = 6$ km.

Between these asymptotic wave-flux limits of $D_w \approx D_L$ at $\hat{h}_m \ll 1$ and $D_w \sim D_{c1}$ at $\hat{h}_m \gg 1$, Figures 10b and 14b also show an intermediate zone at $\hat{h}_m$ ~1–2.5 where D_w

attains maximum mean values and can vacillate. By analogy to surface drag, we refer to this region as a "high-wave-drag" state. However, unlike surface drag, D_w does not exceed D_L in this high-drag range, but instead exceeds the saturated wave-drag D_{c1}, or more accurately, exceeds the limiting D_w at $\hat{h}_m \gg 1$. These wave-drag enhancements are fairly small for the $\beta = 3$ obstacle (presumably due to greater low-level dissipation due to wave breaking) but are on the order of 50% for the axisymmetric obstacle in Figure 10b.

For OMD parameterization, our isolation of the far-field gravity-wave component D_w of the total surface drag D_p in turn defines the component $D_b = D_p - D_w$ that is confined and deposited below $z_i = 6$ km. Figure 17 plots its variation with $\hat{h}_m$ in both normalized and absolute form for both the $\beta = 1$ and $\beta = 3$ obstacles. While D_b is usually referred to as flow-blocking drag in OMD parameterizations, here it likely includes other effects, such as flux deposition due to low-level wave breaking.

Since this study is a first methodical attempt to characterize far-field gravity-wave components of the drag from three-dimensional obstacles at a range of nonlinear $\hat{h}_m$ values, we employed a number of simplifications to make wave characterization easier. One potentially important omission was the Coriolis force ($f = 0$). Ólafsson and Bougeault (1997) compared surface drag in $f = 0$ and $f \neq 0$ simulations and found larger $\hat{D}_p$ values at large $\hat{h}_m$ for $f \neq 0$. They used $a = 40$ km rather than the 10 km value used here. Wells et al. (2008) argued that the primary effect of nonzero f at obstacle widths O(10 km) was to introduce asymmetries to the flow, which trigger vortex shedding that yields larger $\hat{D}_p$ values (e.g. Vosper 2000). For example, Wells et al. (2008) found similar $\hat{D}_p$ between $f \neq 0$ simulations and $f = 0$ simulations in which asymmetry was introduced artifically with a potential temperature perturbation (Schär and Durran 1997). We included neither rotation nor potential

temperature perturbations in these runs to keep our study of wave momentum fluxes as simple as possible. As a result, our drag values may be underestimated at large $\hat{h}_m$. That having been said, our nonlinear simulations yield asymmetric lee vortex evolution after ∼18 hours.

For the $\beta = 3$ obstacle, an additional question for OMD parameterization is how wave momentum fluxes at $\hat{h}_m \gtrsim Fr_c^{-1}$ vary as the angle φ between the incident flow vector and the short axis of the obstacle changes from our value of $\varphi = 0°$. While unable to predict mean magnitudes, Wells et al. (2008) found that the linear drag relations of Phillips (1984) provided a good fit to how surface pressure drag varied as a function of φ for a $\beta = 3$ obstacle at $\hat{h}_m = 2$. They also found a strong D_w/D_p variation with φ, from ∼0.5 at $\varphi = 0°$ to values ∼0.9 at φ near ±90°. Since the latter φ values are equivalent to changing from a $\beta = 3$ to a $\beta = 1/3$ obstacle, Figure 1 predicts for $\hat{h}_m = 2$ and $\beta = 1/3$ that the flow is near the threshold between linear wave and flow-splitting dynamics, for which $D_w/D_p \sim 1$ would be expected based on the current results.

Other omitted processes may also be important in setting gravity wave momentum fluxes. For example, using a no-slip lower boundary condition, Ólafsson and Bougeault (1997) found surface drag reductions at $\hat{h}_m$ ∼1–3 and enhancements at larger $\hat{h}_m$, relative to corresponding free-slip results, although subsequent simulations suggest smaller frictional modifications at large $\hat{h}_m$ (Wells et al. 2005). From our OMD parameterization perspective, we can justify the omission of surface friction here by noting that it is parameterized separately in global models with orographic roughness, land-surface and planetary boundary layer parameterizations. Thus, frictional modifications to parameterized OMD would ideally involve inputs from those schemes that modify a frictionless baseline OMD parameterization. In practice, however, current OMD parameterizations in models are not modified by frictional inputs.

As a result, the model-tuned values of Fr_c^{-1} ∼0.25–0.375 used in some OMD parameterizations, which significantly underestimate the gravity wave momentum fluxes reported here, may parameterize the mean overall effect of friction and other omitted processes in reducing far-field wave fluxes. Thus, future investigations of the influence of friction, φ, and other omitted processes on wave momentum fluxes at nonlinear Froude numbers would clearly be worthwhile.

6. Summary

Using WRF model simulations, we studied mesoscale dynamics resulting from a steady unsheared flow impinging upon an idealized obstacle (1) of along-stream width $a = 10$ km and cross-stream width $b = \beta a$. We focused on an axisymmetric ($\beta = 1$) and elliptical ($\beta = 3$) obstacle, and for each performed experiments in which the normalized obstacle height $\hat{h}_m = Fr^{-1}$ was progressively increased from the linear regime ($\hat{h}_m \ll 1$) through to the highly nonlinear regime ($\hat{h}_m \gg 1$), as shown in Figure 1. The primary foci of our analysis were the local and areally-integrated momentum fluxes of the far-field equilibrium gravity wave fields that propagated to a height of 6 km. Those fluxes were quantified both directly from the WRF velocity anomalies and indirectly using diagnostic Fourier-transform methods. We sought mean results that could be used to specify gravity-wave momentum fluxes in subgrid-scale orographic mesoscale drag (OMD) parameterizations in global weather and climate models. Our major findings are summarized schematically in Figure 18.

Since many OMD parameterizations assign wave momentum fluxes by scaling surface pressure drag, Figure 18a first summarizes the bulk properties of (normalized) pressure drag

as a function of $\hat{h}_m$. At $\hat{h}_m < Fr_c^{-1}$ pressure drag is close to linear hydrostatic predictions ($\hat{D}_p \sim 1$) and translates fully into propagating gravity wave momentum flux at 6 km. At $Fr_c^{-1} < \hat{h}_m \lesssim 2$ high-drag wave-breaking states ($\hat{D}_p > 1$) occur, with the Fr_c^{-1} threshold predicted to within ∼10% for both the $\beta = 1$ and $\beta = 3$ obstacle using the Smith (1989b) curves in Figure 1. Surface drag for the $\beta = 3$ obstacle vacillates in the $\hat{h}_m$ ∼0.7–3 range due to cyclical buildup and breakdown of wave activity, with the period and amplitude of these vacillations decreasing with increasing $\hat{h}_m$. Periodic drag vacillation occurred for the axisymmetric obstacle only at $\hat{h}_m = 1.2$. At $\hat{h}_m \gtrsim$2–3 pressure drag decreased smoothly with time to normalized equilibrium values that were almost identical for both obstacles, and were well fitted as $\hat{h}_m^{-1.3}$.

Mean features in the areally-integrated wave momentum fluxes, or "wave drag," at $z_i =$ 6 km are summarized in absolute (unnormalized) form in Figure 18b. In the linear $\hat{h}_m < Fr_c^{-1}$ range, wave drag D_w matches both D_p and D_L and thus varies according to the latter's analytical $\hat{h}_m^2$ dependence in (13). While at $\hat{h}_m \gtrsim Fr_c^{-1}$ D_w suddenly becomes a significantly smaller fraction of the total pressure drag (see Figure 16), absolute values peak in the high-drag range $Fr_c^{-1} < \hat{h}_m \lesssim 2$. As with pressure drag, wave drag vacillates in this range due to periodic buildup and breakdown of wave amplitudes just above the obstacle (see Figure 4).

At $\hat{h}_m \gtrsim$2–3 wave drag levels off to a constant value, which is quantified to within 10-40% by a "saturated" clipped wave drag D_{c1} given by the analytical relation (21) using $\alpha = Fr_{cs}^{-1} \approx 1$. Stable invariant wave drag in this high–$\hat{h}_m$ range is a surprising finding, given that the three-dimensional distribution of wave momentum flux varies appreciably with $\hat{h}_m$ over this range (see Figure 8) and can be additionally impacted by nonstationary wave responses in the elliptical obstacle simulations (see Figure 12). We show that the analytical

relation D_{c1} arises here from a demonstrably incorrect model of the $\hat{h}_m \gtrsim Fr_c^{-1}$ wave field. Nonetheless, based on the agreement in Figure 18b, it offers a simple and convenient way of accurately quantifying wave flux in this nonlinear $\hat{h}_m$ range. Mean wave-drag curves like those in Figure 18b can easily be incorporated into existing OMD parameterizations, given their close current associations with the mean drag properties of idealized three-dimensional obstacles (see, e.g., Scinocca and McFarlane 2000).

Indeed, some current OMD parameterizations already use analogues of $D_w \sim D_{c1}$ to assign wave momentum fluxes at nonlinear Froude numbers. While we found best agreement using Fr_{cs}^{-1} =1–1.2, the values of Fr_c^{-1} ($\approx Fr_{cs}^{-1}$) used in OMD parameterizations that have been "tuned" to optimize model skill are currently ∼0.25–0.375, which, based on our results, imply order-of-magnitude underestimates of parameterized orographic gravity wave momentum fluxes at $\hat{h}_m > Fr_c^{-1}$ in such models. However, our model simulations do not include additional effects like surface friction and rotation which may reduce wave fluxes. Our results also show large vacillations in both surface and wave drag, particularly in the range $Fr_c^{-1} < \hat{h}_m \lesssim$2–3, which existing schemes do not include, but could, for example, via an explicitly stochastic parameterization of OMD (see, e.g., Palmer 2001).

Acknowledgments.

This research was supported by the Office of Naval Research's base 6.1 research program at the Naval Research Laboratory, by NASA GMAP contract NNTG06HM19I, and by the National Science Foundation through grants ATM-0435789 (DB) and ATM-0448888 (JL).

APPENDIX A

Analytical Wave Drag Relations Based on the Dividing Streamline Concept

We consider waves forced by flow over a "clipped" obstacle $h_c(x, y)$ located between the dividing streamline z_{ds} and the obstacle peak h_m (Lindeman et al. 2008). The simplest derivation assumes the same shape as the unclipped obstacle, same widths a and b, but reduced height $(h_c)_m = h_m - z_{ds}$ given by (20). Assuming the linear hydrostatic solution D_L holds at $0 \leq \hat{h}_m \leq \alpha$, then at $\hat{h}_m > \alpha$ the wave drag is

$$D_{c1} = D_L \left[\frac{(h_c)_m}{h_m} \right]^2 = D_L \alpha^2 \hat{h}_m^{-2} = B(\beta) a \rho_0 \alpha^2 \frac{U^3}{N}. \tag{A1}$$

In reality the clipped mountain peak is narrower and generates much shorter-scale waves (Ding et al. 2003; Lindeman et al. 2008). A better approximation then might be to assume that the effective half widths a_c and b_c of the clipped obstacle $h_c(x, y)$ reduce linearly with the clipping height so that the obstacle's height-to-width ratio remains constant. Ignoring possible nonhydrostatic effects as a_c and b_c contract, this yields a clipped wave-drag

$$D_{c2} = D_L \alpha^3 \hat{h}_m^{-3}. \tag{A2}$$

In fact, neither approximation fits the actual solution D_c from the Fourier-ray calculation (large triangles in Figure 10), which is most closely fitted at $\hat{h}_m > \alpha$ as $D_L \hat{h}_m^{-2.5}$, essentially halfway between approximations (A1) and (A2).

REFERENCES

Aguilar, D. A. and B. R. Sutherland, 2006: Internal wave generation from rough topography. *Phys. Fluids*, **18**, 066 603.

Bacmeister, J. T. and M. R. Schoeberl, 1989: Breakdown of vertically propagating two-dimensional gravity waves forced by orography. *J. Atmos. Sci.*, **46**, 2109–2134.

Baines, P. G., 1995: *Topographic effects in stratified flows*. Cambridge University Press, 492 pp.

Bauer, M. H., G. J. Mayr, I. Vergeiner, and H. Pichler, 2000: Strongly nonlinear flow over and around a three-dimensional mountain as a function of the horizontal aspect ratio. *J. Atmos. Sci.*, **57**, 3971–3991.

Broutman, D., S. D. Eckermann, and J. W. Rottman, 2009: Practical application of two turning-point theory to mountain-wave transmission through a wind jet. *J. Atmos. Sci.*, **66**, 481–494.

Broutman, D., J. Ma, S. D. Eckermann, and J. Lindeman, 2006: Fourier-ray modeling of transient trapped lee waves. *Mon. Wea. Rev.*, **143**, 2849–2856.

Broutman, D., J. W. Rottman, and S. D. Eckermann, 2002: Maslov's method for stationary hydrostatic mountain waves. *Quart. J. Roy. Meteor. Soc.*, **128**, 1159–1172.

Broutman, D., J. W. Rottman, and S. D. Eckermann, 2003: A simplified Fourier method for nonhydrostatic mountain waves. *J. Atmos. Sci.*, **60**, 2686–2696.

Ding, L., R. A. Calhoun, and R. L. Street, 2003: Numerical simulation of strongly stratified flow over a three-dimensional hill. *Bound.-Layer Meteor.*, **107**, 81–114.

Dupont, P., Y. Kadri, and J.-M. Chomaz, 2001: Internal waves generated by the wake of Gaussian hills. *Phys. Fluids*, **13**, 3223–3233.

Durran, D. R., 1995: Pseudomomentum diagnostics for two-dimensional stratified compressible flows. *J. Atmos. Sci.*, **52**, 3997–4009.

Epifanio, C. C. and D. R. Durran, 2001: Three-dimensional effects in high-drag-state flows over long ridges. *J. Atmos. Sci.*, **58**, 1051–1065.

Gregory, D., G. J. Shutts, and J. R. Mitchell, 1998: A new gravity-wave-drag scheme incorporating anisotropic orography and low-level wave breaking: Impact upon the climate of the UK Meteorological Office Unified Model. *Quart. J. Roy. Meteor. Soc.*, **124**, 463–493.

Hunt, J. C. R. and W. H. Snyder, 1980: Experiments on stably and neutrally stratified flow over a model three dimensional hill. *J. Fluid Mech.*, **96**, 671–704.

Klemp, J. B., J. Dudhia, and A. D. Hassiotis, 2008: An upper gravity-wave absorbing layer for NWP applications. *Mon. Wea. Rev.*, **136**, 3987–4004.

Klemp, J. B. and D. K. Lilly, 1980: Mountain waves and momentum flux. *Orographic effects in planetary flows*, R. Hide and P. W. White, Eds., ICSU/WMO, GARP Publication Series, Vol. 23, 116–141.

Lindeman, J., 2008: A numerical study of topographical effects on flow regimes in the lower atmosphere. Ph.D. thesis, George Mason University, 151 pp.

Lindeman, J., D. Broutman, S. D. Eckermann, J. Ma, J. W. Rottman, and Z. Boybeyi, 2008: Mesoscale model initialization of the Fourier method for mountain waves. *J. Atmos. Sci.*, **65**, 2749–2756.

Lott, F. and M. J. Miller, 1997: A new subgrid-scale orographic drag parametrization: Its formulation and testing. *Quart. J. Roy. Meteor. Soc.*, **123**, 101–127.

McLandress, C. and J. F. Scinocca, 2005: The GCM response to current parameterizations of non-orographic gravity wave drag. *J. Atmos. Sci.*, **62**, 2394–2413.

Mercier, M. J., N. B. Garnier, and T. Dauxois, 2008: Reflection and diffraction of internal waves analyzed with the Hilbert transform. *Phys. Fluids*, **118**, 086 601.

Miranda, P. M. A. and I. N. James, 1992: Non-linear three-dimensional effects on gravity-wave drag: Splitting flow and breaking waves. *Quart. J. Roy. Meteor. Soc.*, **118**, 1057–1081.

Ólafsson, H. and P. Bougeault, 1996: Nonlinear flow past an elliptic mountain ridge. *J. Atmos. Sci.*, **53**, 2465–2489.

Ólafsson, H. and P. Bougeault, 1997: The effect of rotation and surface friction on orographic drag. *J. Atmos. Sci.*, **54**, 193–210.

Palmer, T. N., 2001: A nonlinear dynamical perspective on model error: A proposal for

non-local stochastic-dynamic parametrization in weather and climate prediction models. *Quart. J. Roy. Meteor. Soc.*, **127**, 279–304.

Phillips, D. S., 1984: Analytical surface pressure and drag for linear hydrostatic flow over three-dimensional elliptical mountains. *J. Atmos. Sci.*, **112**, 1073–1084.

Satomura, T. and K. Sato, 1999: Secondary generation of gravity waves associated with the breaking of mountain waves. *J. Atmos. Sci.*, **56**, 3847–3858.

Schär, C. and D. R. Durran, 1997: Vortex formation and vortex shedding in continuously stratied flows past isolated topography. *J. Atmos. Sci.*, **54**, 534–554.

Scinocca, J. F. and N. A. McFarlane, 2000: The parameterization of drag induced by stratified flow over anisotropic orography. *Quart. J. Roy. Meteor. Soc.*, **126**, 2353–2393.

Scinocca, J. F., N. A. McFarlane, M. Lazare, J. Li, and D. Plummer, 2008: The CCCma third generation AGCM and its extension into the middle atmosphere. *Atmos. Chem. Phys.*, **126**, 7055–7074.

Skamarock, W. C., et al., 2008: A description of the advanced research WRF version 3. NCAR Tech. Note NCAR/TN–475+STR, NCAR, 113 pp.

Smith, R. B., 1980: Linear theory of stratified hydrostatic flow past an isolated mountain. *Tellus*, **32**, 348–364.

Smith, R. B., 1988: Linear theory of stratified flow past an isolated mountain in isosteric coordinates. *J. Atmos. Sci.*, **45**, 3889–3896.

Smith, R. B., 1989a: Hydrostatic air-flow over mountains. *Adv. Geophys.*, **31**, 1–41.

Smith, R. B., 1989b: Mountain-induced stagnation points in hydrostatic flow. *Tellus*, **41A**, 270–274.

Smith, S. A., J. D. Doyle, A. R. Brown, and S. Webster, 2006: Sensitivity of resolved mountain drag to model resolution for MAP case-studies. *Quart. J. Roy. Meteor. Soc.*, **132**, 1467–1487.

Smolarkiewicz, P. K. and R. Rotunno, 1989: Low Froude number flow past three-dimensional obstacles. Part i: Baroclinically generated lee vortices. *J. Atmos. Sci.*, **46**, 1154–1164.

Snyder, W. H., R. S. Thompson, R. E. Eskridge, R. E. Lawson, I. P. Castro, J. T. Lee, J. C. R. Hunt, and Y. Ogawa, 1985: The structure of strongly stratified flow over hills: dividing streamline concept. *J. Fluid Mech.*, **152**, 249–288.

Stein, J., 1992: Investigation of the regime diagram of hydrostatic flow over a mountain with a primitive equation model. Part i: Two-dimensional flows. *Mon. Wea. Rev.*, **120**, 2962–2976.

Tan, K. A. and S. D. Eckermann, 2000: Numerical model simulations of mountain waves in the middle atmosphere over the southern Andes. *Atmospheric Science Across the Stratopause*, D. E. Siskind, S. D. Eckermann, and M. E. Summers, Eds., American Geophysical Union, AGU Monograph Series, Vol. 123, 311–318.

Vosper, S. B., 2000: Three-dimensional numerical simulations of strongly stratified flow past conical orography. *J. Atmos. Sci.*, **57**, 3716–3739.

Vosper, S. B., I. P. Castro, W. H. Snyder, and S. D. Mobbs, 1999: Experimental studies of strongly stratified flow past three-dimensional orography. *J. Fluid Mech.*, **390**, 223–249.

Webster, S., A. R. Brown, D. R. Cameron, and C. P. Jones, 2003: Improvements to the representation of orography in the Met Office Unified Model. *Quart. J. Roy. Meteor. Soc.*, **129**, 1989–2010.

Welch, W. T., P. K. Smolarkiewicz, R. Rotunno, and B. A. Boville, 2001: The large-scale effects of flow over periodic mesoscale topography. *J. Atmos. Sci.*, **58**, 1477–1492.

Wells, H., S. B. Vosper, A. N. Ross, A. R. Brown, and S. Webster, 2008: Wind direction effects on orographic drag. *Quart. J. Roy. Meteor. Soc.*, **134**, 689–701.

Wells, H., S. Webster, and A. Brown, 2005: The effect of rotation on the pressure drag force produced by flow around long mountain ridges. *Quart. J. Roy. Meteor. Soc.*, **131**, 1321–1338.

List of Figures

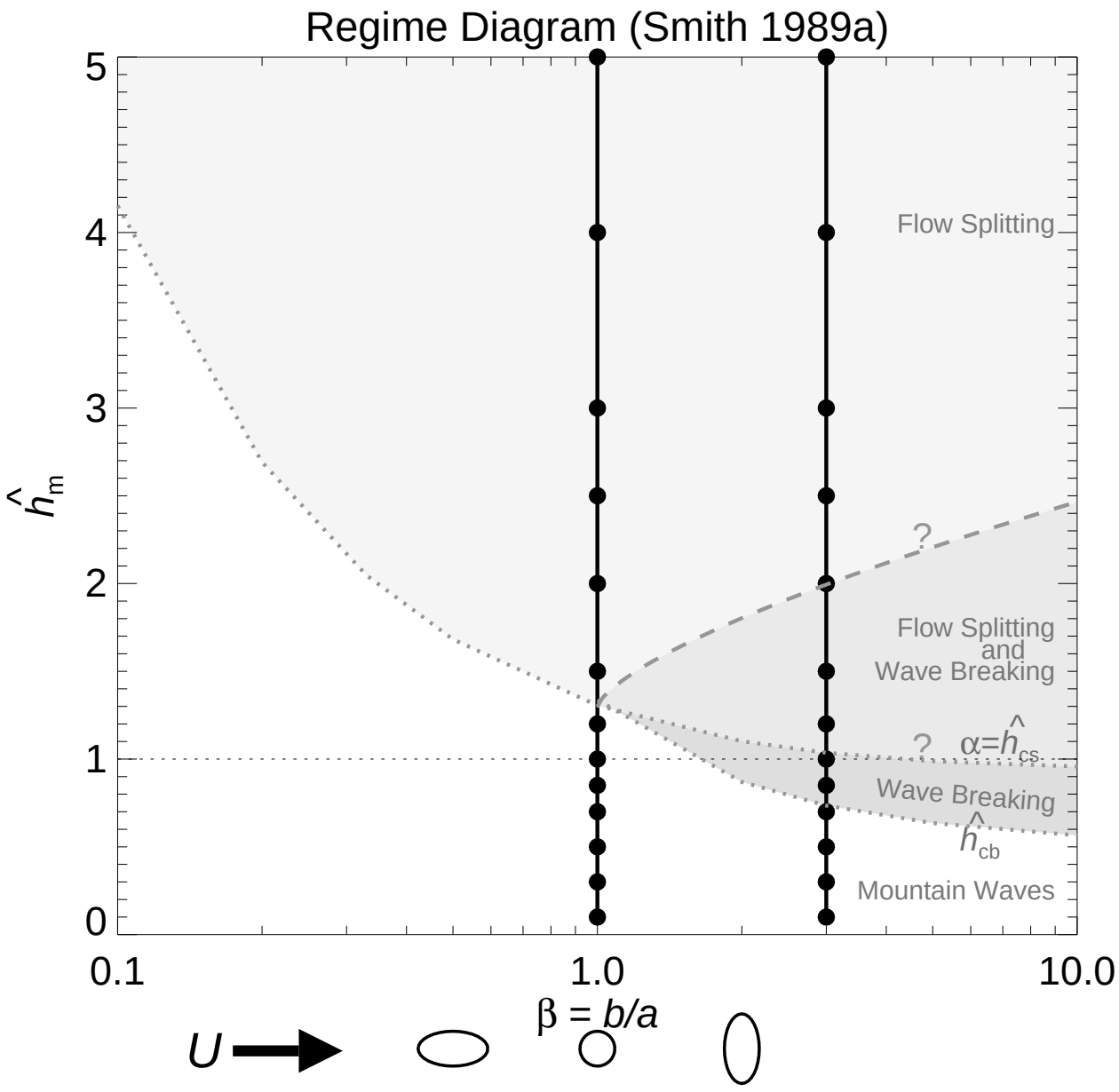

FIG. 1. Regime diagram delineating mesoscale dynamical responses to flow U across the elliptical obstacle (1) as a function of $\hat{h}_m$ and β, following Smith (1989a,b). Solid circles show $(\hat{h}_m, \beta)$ values whose dynamics we model in this study. Dotted gray curves show critical values for onset of wave breaking ($\hat{h}_m > \hat{h}_{cb} = Fr_{cb}^{-1}$) and flow splitting ($\hat{h}_m > \hat{h}_{cs} = Fr_{cs}^{-1} = \alpha$).

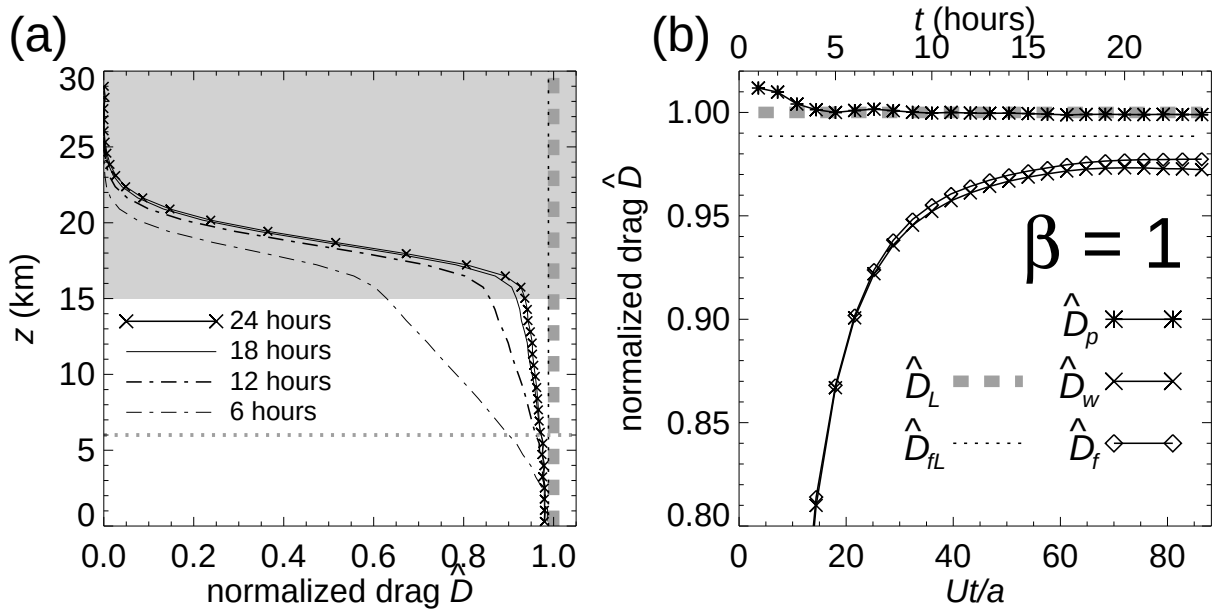

FIG. 2. Nondimensional drag for obstacle of $\beta = 1$ and $\hat{h}_m = 0.1$: (a) vertical profiles of $\hat{D}_w$ at 6, 12, 18 and 24 hours. Gray region shows sponge layer. Horizontal dotted line shows $z_i = 6$ km where $\hat{D}_w$ and $\hat{D}_f$ are evaluated and plotted in (b) as time series together with surface pressure drag $\hat{D}_p$ and the linear $t \to \infty$ predictions $\hat{D}_L$ and $\hat{D}_f$.

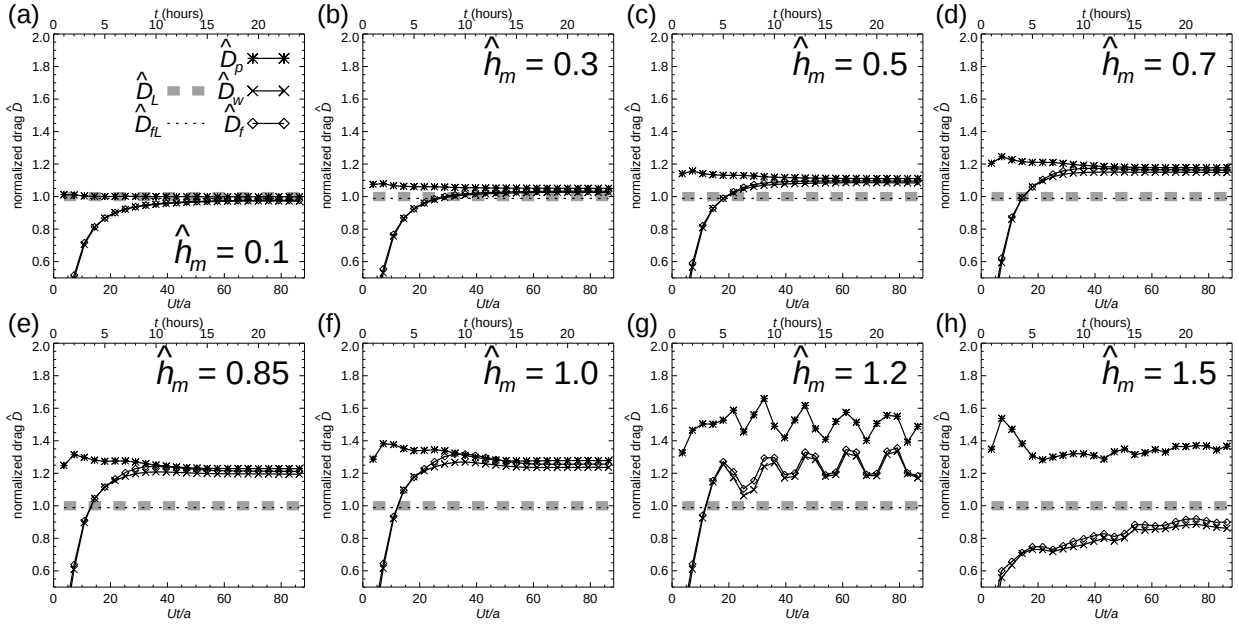

FIG. 3. Nondimensional drag as a function of time for the $\beta = 1$ obstacle for normalized obstacle heights $\hat{h}_m$ ranging from (a) 0.1 to (h) 1.5. The various drag curves are labeled at the top of panel (a). See text for symbol definitions.

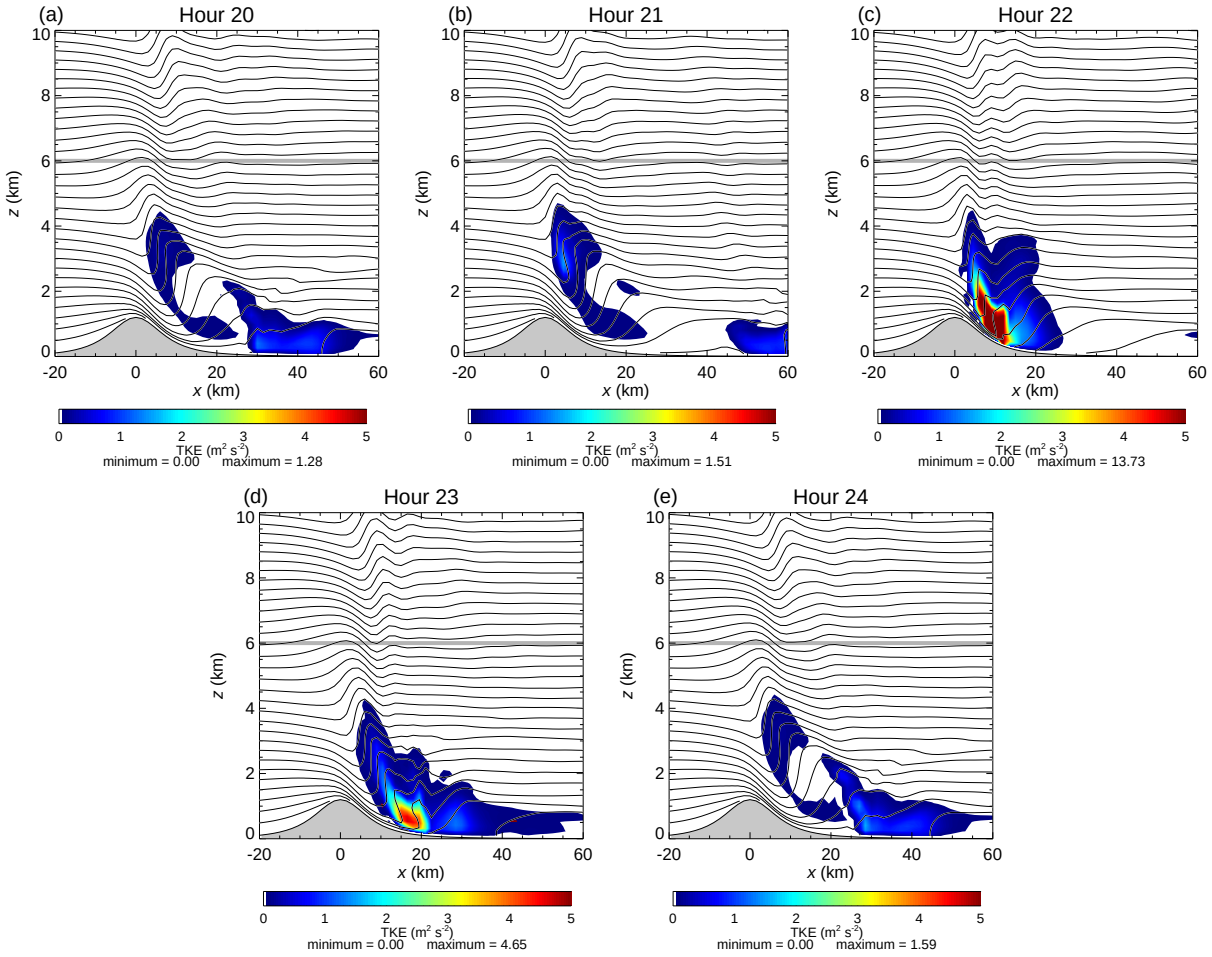

FIG. 4. Isentropes as a function of x and z (1 K contour interval) along the central obstacle axis ($y = 0$) at hourly intervals from 20-24 hours for $\hat{h}_m = 1.2$ and $\beta = 1$. Color shading shows turbulent kinetic energy (units $\mathrm{m}^2\ \mathrm{s}^{-2}$: see color bar). Gray line depicts $z_i = 6$ km where gravity wave momentum fluxes are computed.

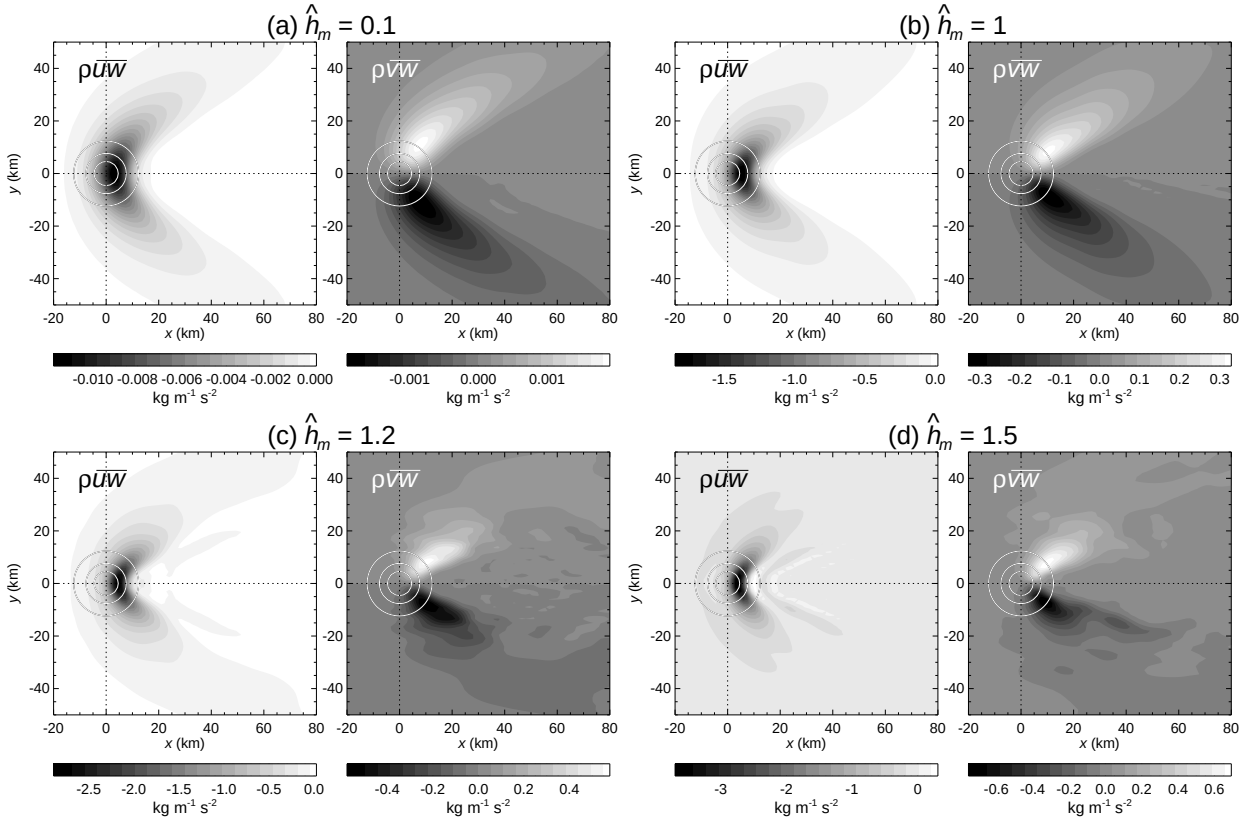

FIG. 5. Each panel pair plots the FT-based $\rho\overline{uw}$ and $\rho\overline{vw}$ fields for the $\beta = 1$ obstacle at 6 km altitude after 24 hours, for $\hat{h}_m$ values of (a) 0.1, (b) 1.0, (c) 1.2, and (d) 1.5. Flux units in each accompanying color bar are kg m^{-1} s^{-2}.

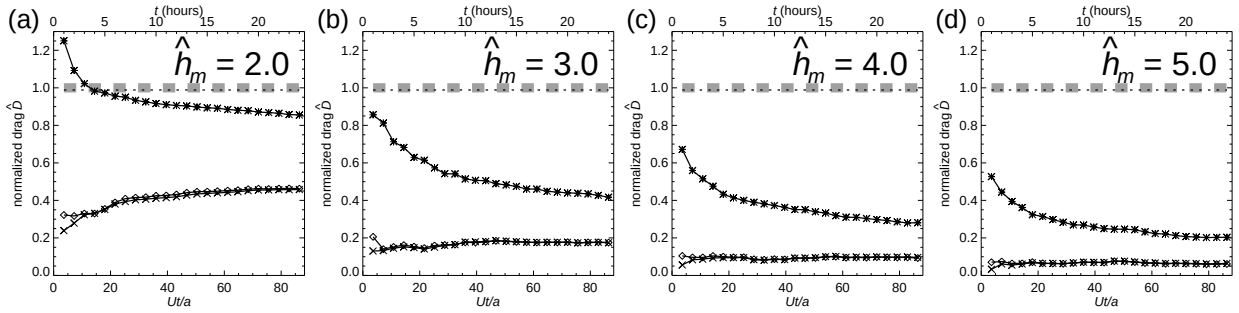

FIG. 6. Nondimensional drag as a function of time for the $\beta = 1$ obstacle for normalized obstacle heights $\hat{h}_m$ ranging from (a) 2.0 to (d) 5.0. Curve definitions are as given in Figure 3a.

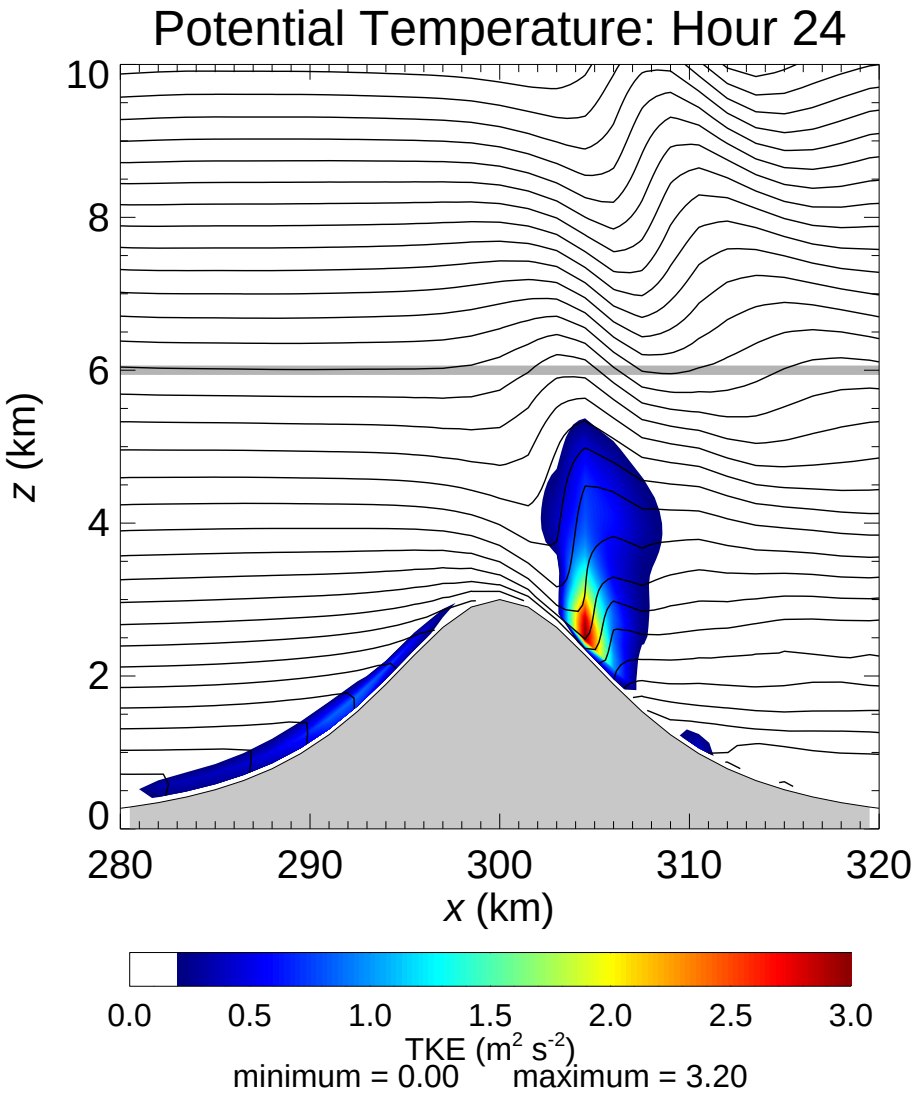

FIG. 7. Isentropes as a function of x and z (1 K contour interval) along the central obstacle axis ($y = 0$) at hour 24 for $\hat{h}_m = 3$ and $\beta = 1$. Color shading shows turbulent kinetic energy (units $m^2\ s^{-2}$: see color bar). Gray line depicts $z_i = 6$ km where gravity wave momentum fluxes are computed.

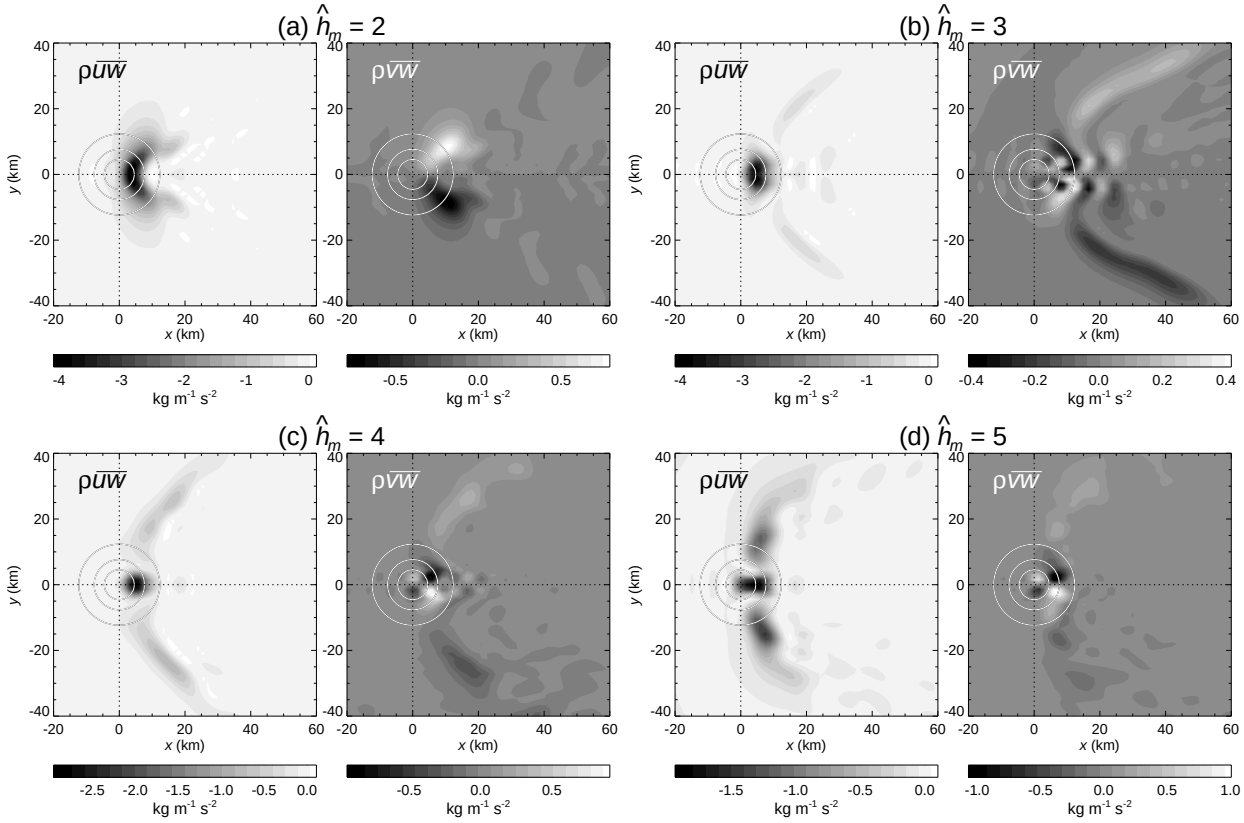

FIG. 8. As in Figure 5 but for $\hat{h}_m$ values of (a) 2.0, (b) 3.0, (c) 4.0, and (d) 5.0.

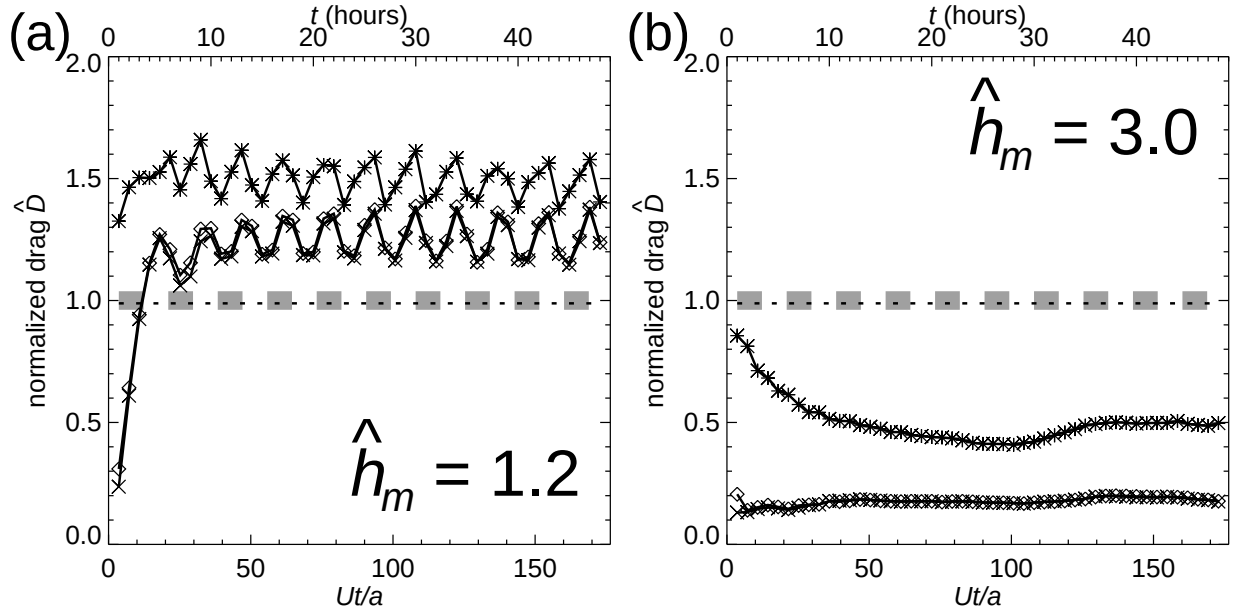

FIG. 9. Nondimensional drag as a function of time out to 48 hours for the $\beta = 1$ obstacle for normalized obstacle heights $\hat{h}_m$ of (a) 1.2 and (d) 3.0. Curve definitions are given in Figure 3a.

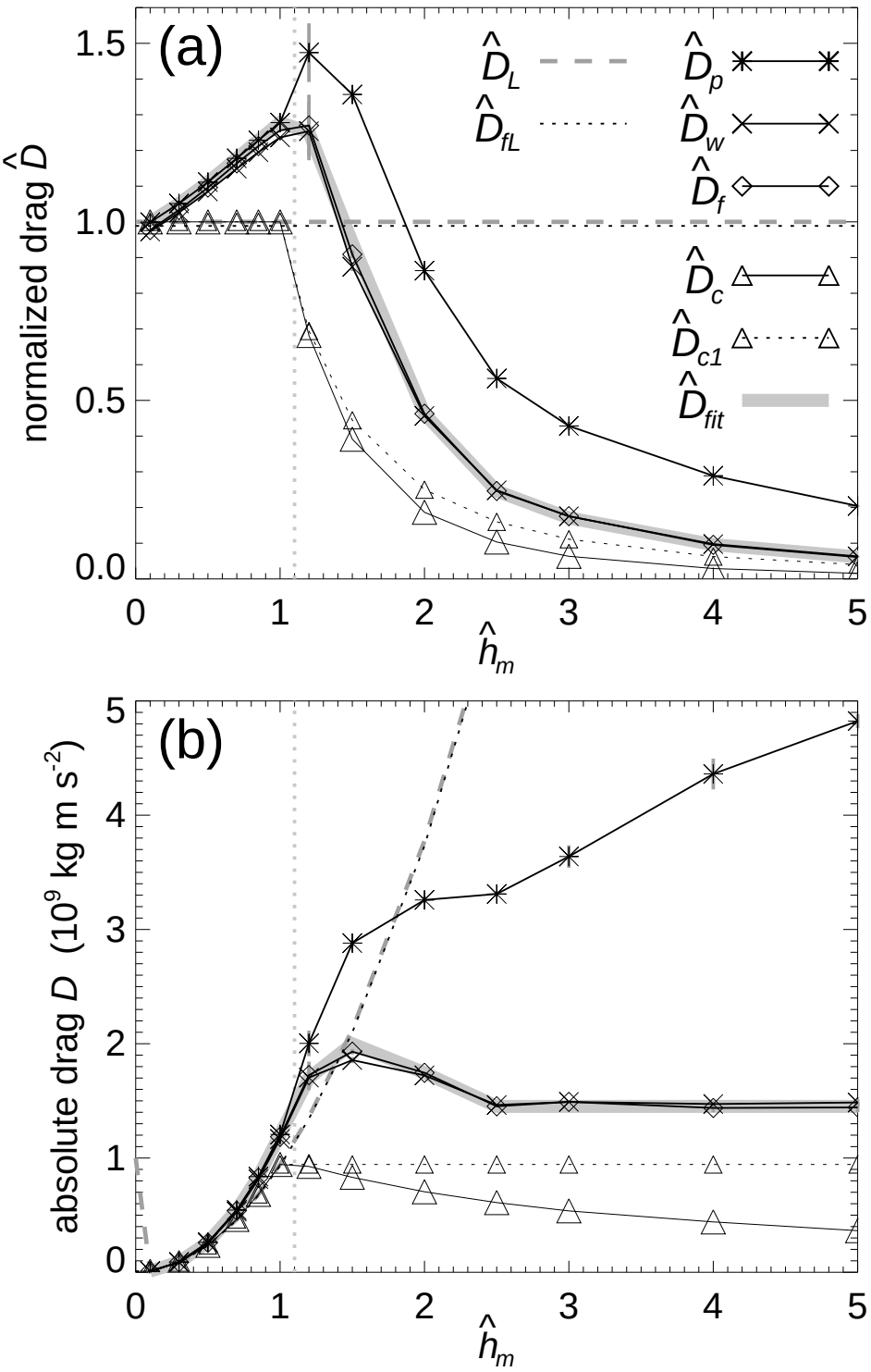

FIG. 10. (a) Nondimensional and (b) absolute mean drag (t =20–24 hours) and range (gray error bars) versus $\hat{h}_m$ for $\beta = 1$ WRF simulations. Dotted gray line at $\hat{h}_m \sim 1.1$ demarks responses with and without TKE at smaller and larger $\hat{h}_m$, respectively. The various drag terms are labeled top right: see text for symbol definitions.

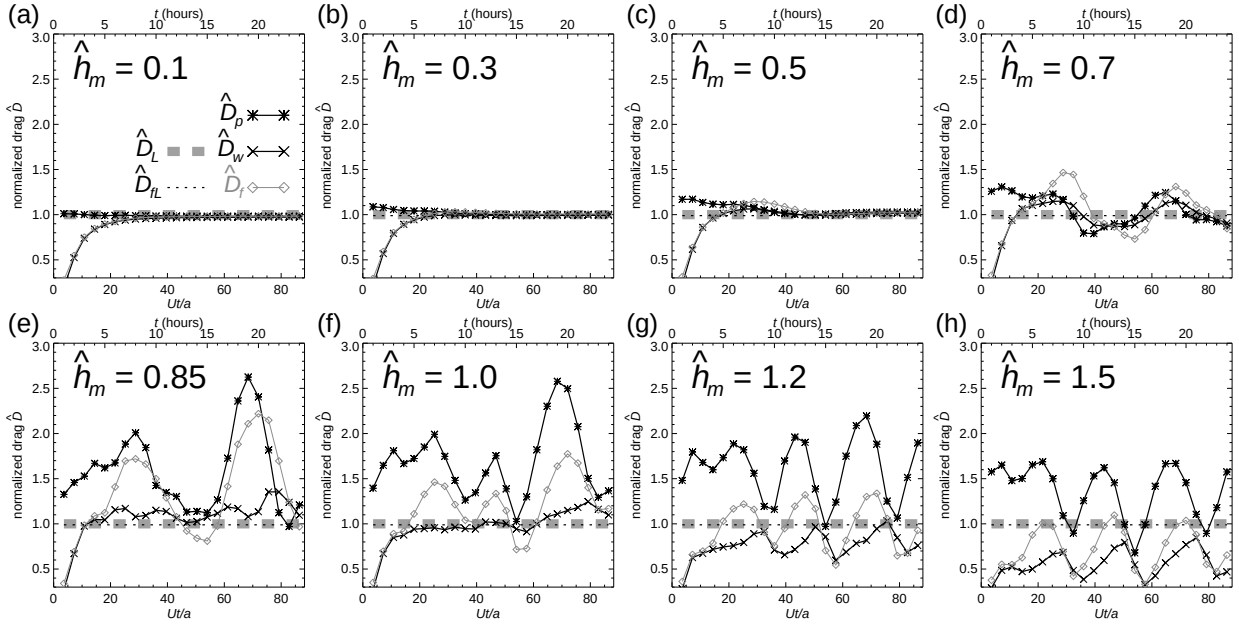

FIG. 11. Nondimensional drag as a function of time for the $\beta = 3$ obstacle for normalized obstacle heights $\hat{h}_m$ ranging from (a) 0.1 to (h) 1.5. The various drag curves are labeled at the top of panel (a). See text for symbol definitions.

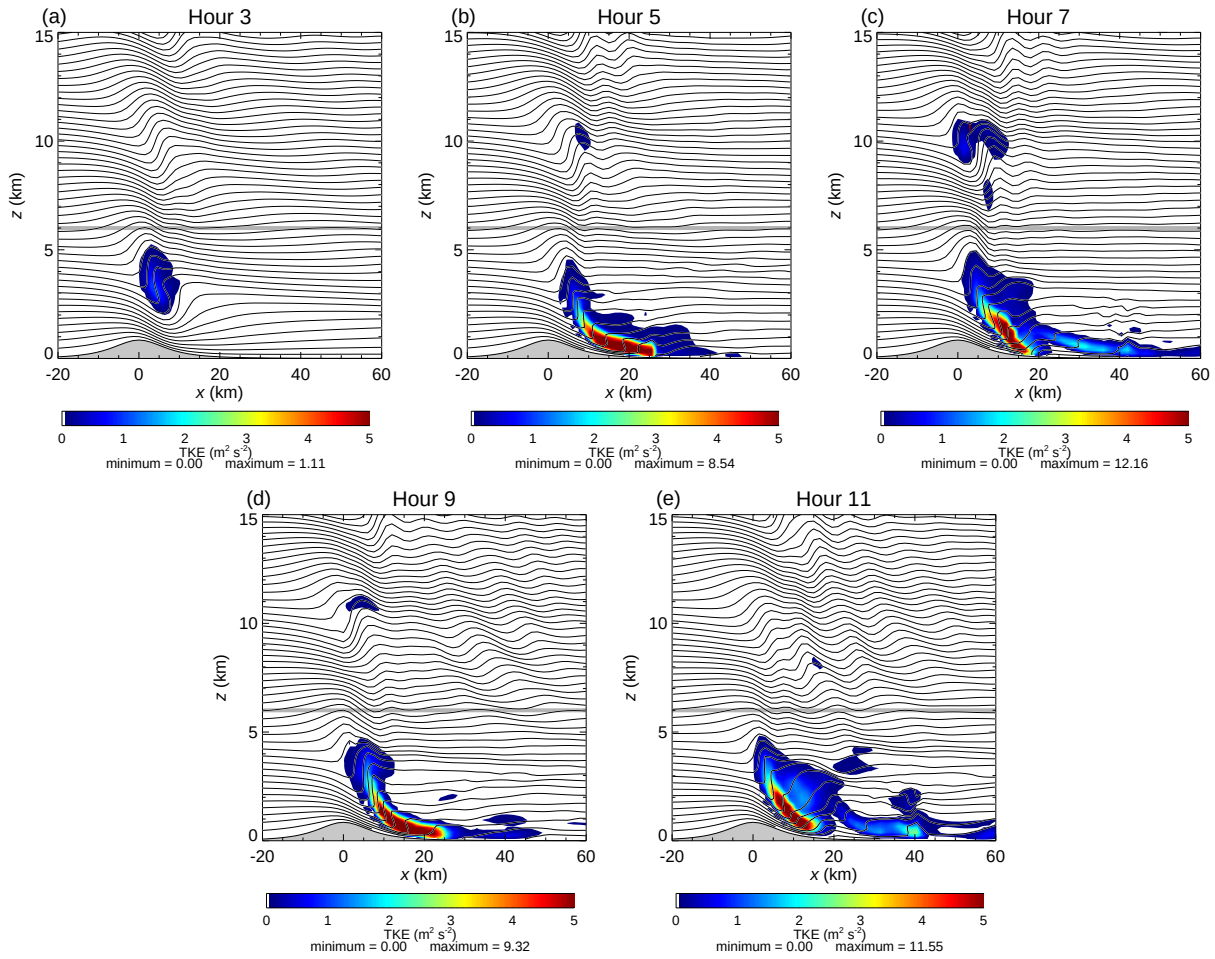

FIG. 12. Isentropes as a function of x and z (1 K contour interval) along the central obstacle axis ($y = 0$) at hours 3, 5, 7, 9 and 11 for $\hat{h}_m = 0.85$ and $\beta = 3$. Color shading shows areas of turbulent kinetic energy (units m^2 s^{-2}: see color bar). Gray line depicts $z_i = 6$ km where gravity wave momentum fluxes are computed.

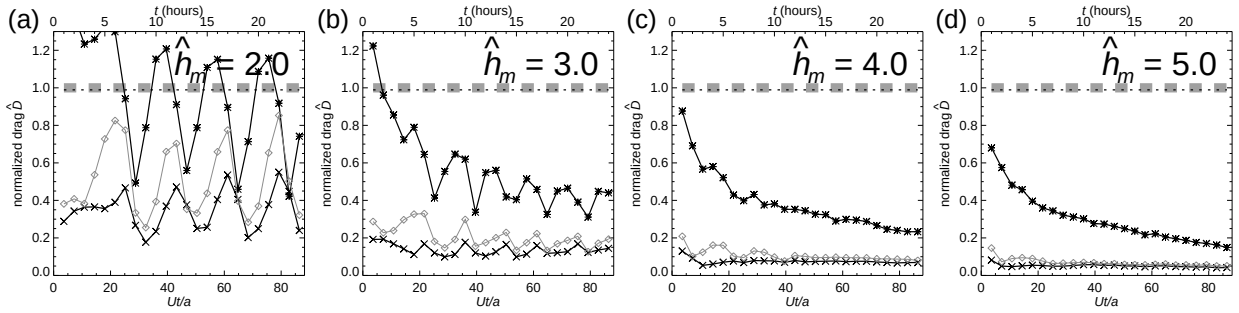

FIG. 13. Nondimensional drag as a function of time for the $\beta = 3$ obstacle for normalized obstacle heights $\hat{h}_m$ ranging from (a) 2.0 to (d) 5.0. Curve definitions are as given in Figure 11a.

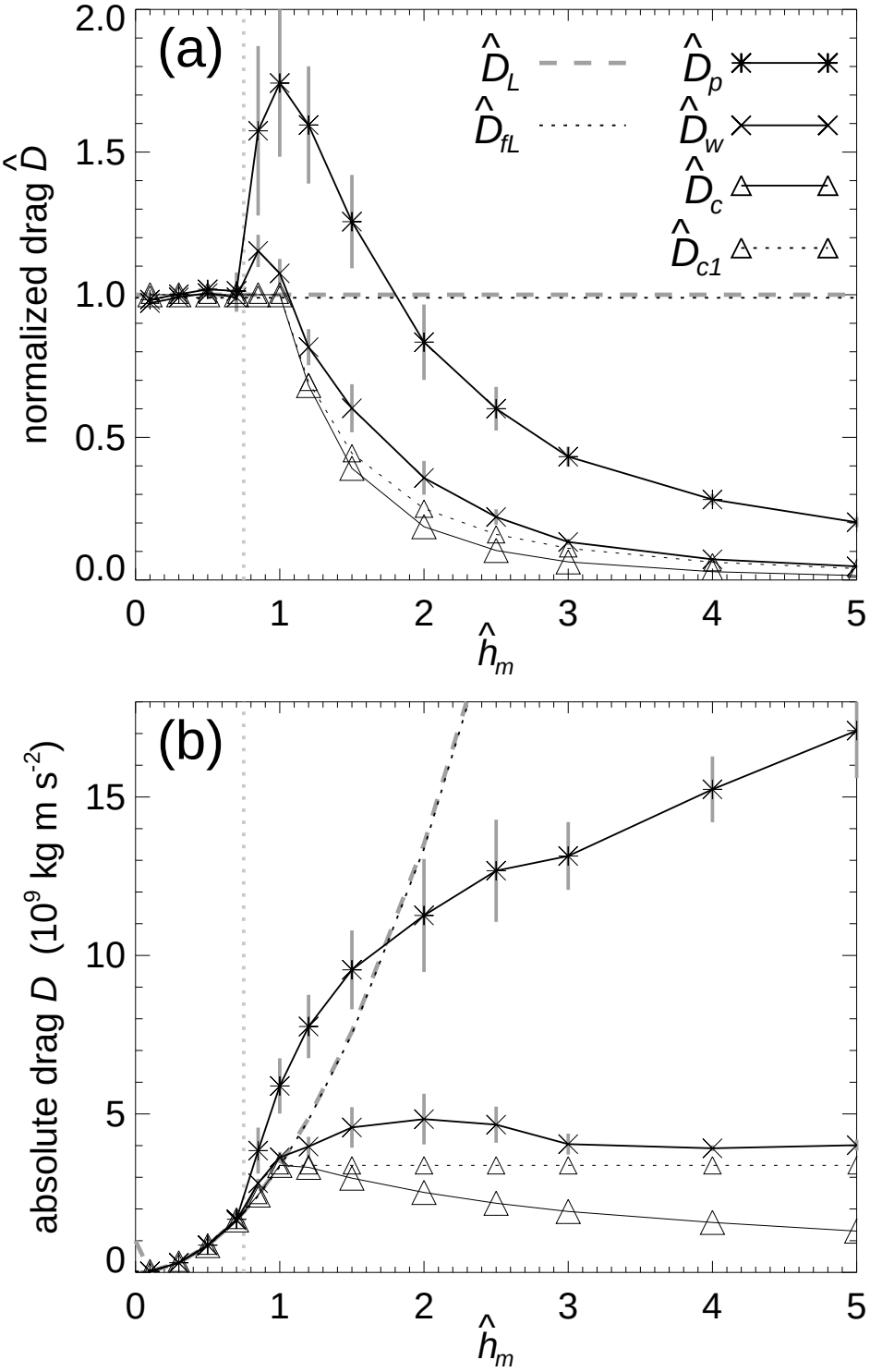

FIG. 14. (a) Nondimensional and (b) absolute mean drag (t =12–24 hours) and standard deviations (gray error bars) versus $\hat{h}_m$ for $\beta = 3$ WRF simulations. Dotted gray line at $\hat{h}_m \sim 0.7$ demarks responses with and without TKE at smaller and larger $\hat{h}_m$, respectively. The various drag terms are labeled top right: see text for symbol definitions.

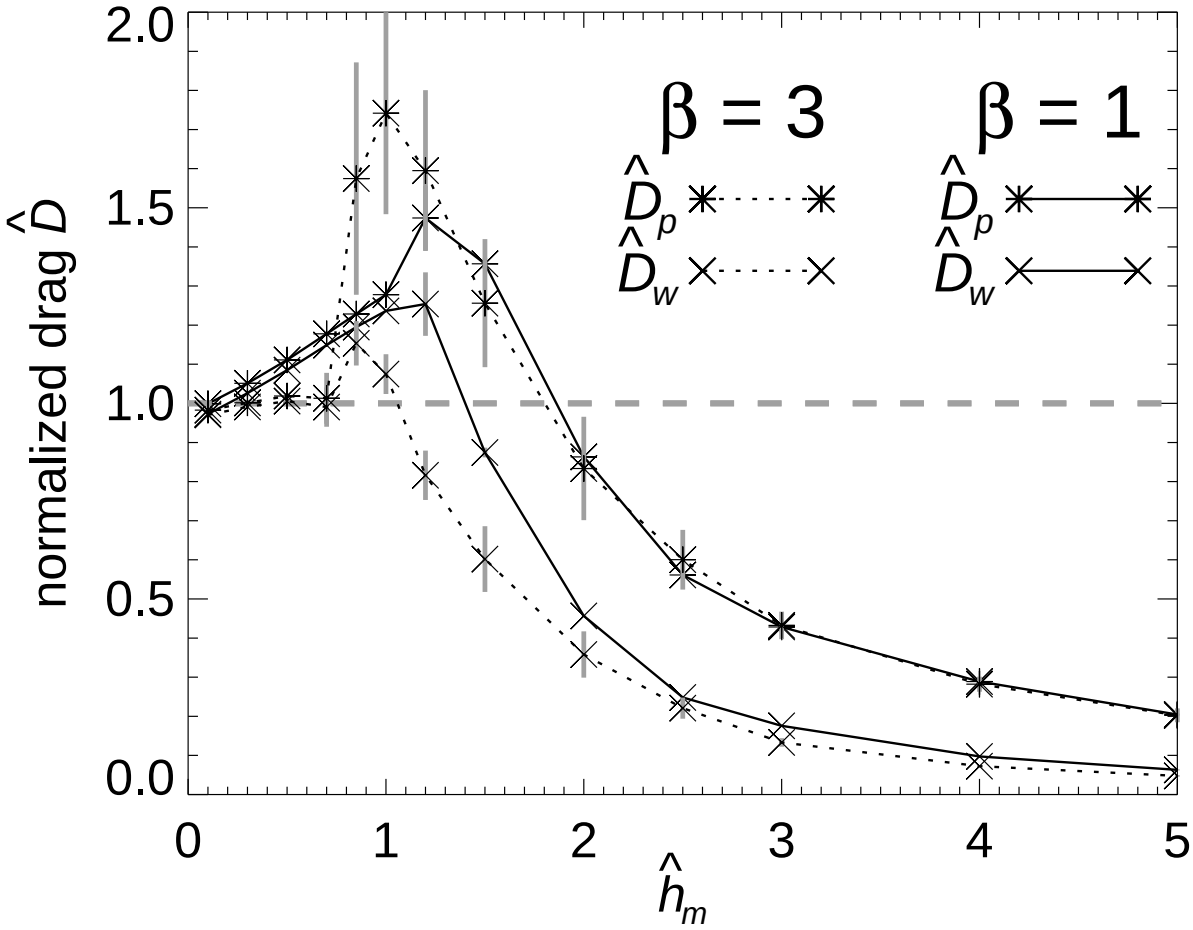

FIG. 15. (a) Nondimensional mean surface pressure drag and wave drag versus $\hat{h}_m$ for the $\beta = 1$ (solid) and $\beta = 3$ (dotted) obstacles.

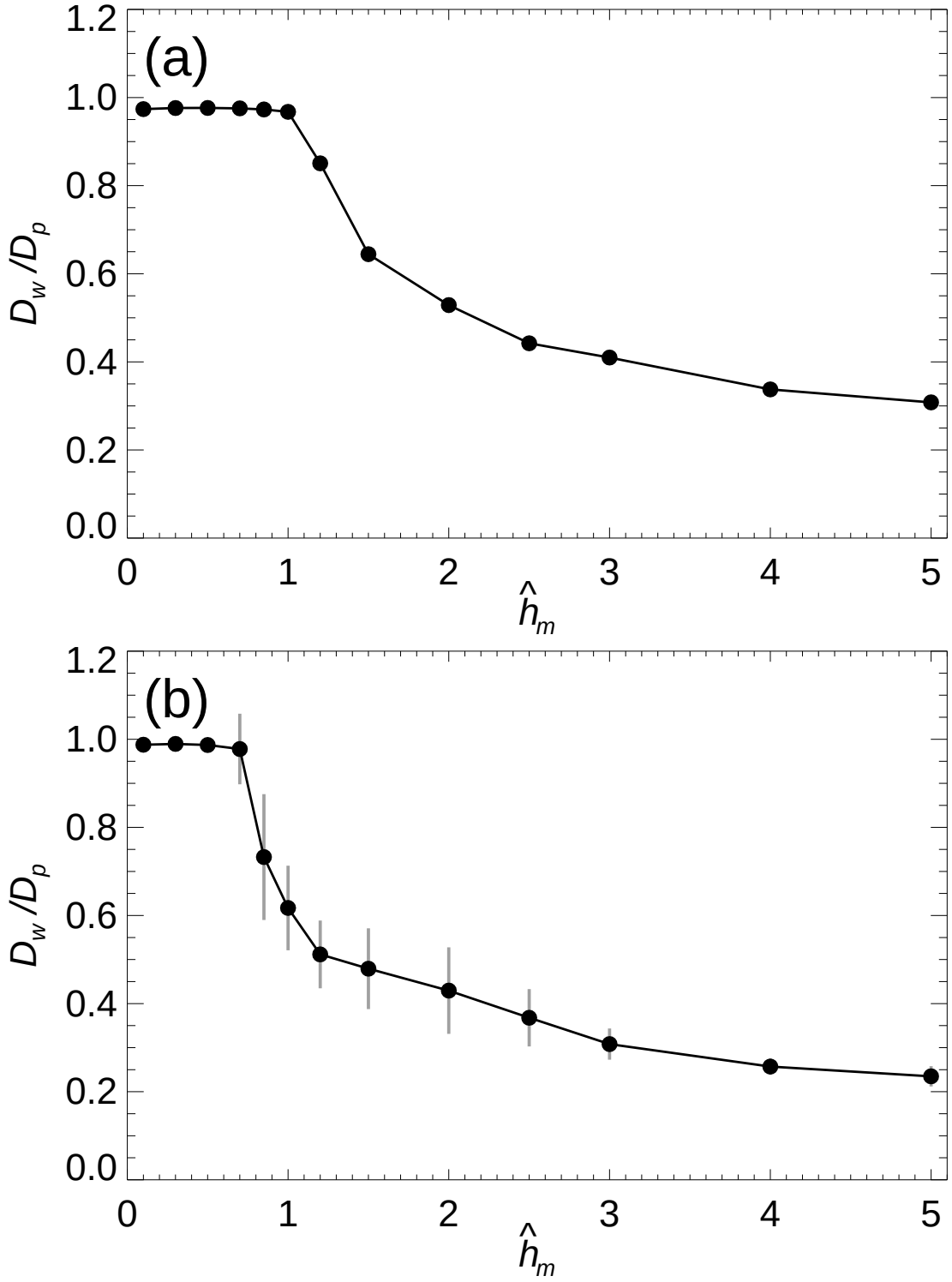

FIG. 16. (Solid) ratio of wave drag D_w at 6 km to surface pressure drag D_p for (a) $\beta = 1$ and (b) $\beta = 3$ obstacle. Standard deviations in (b) were derived from the individual standard deviations of D_w and D_p in Figure 14.

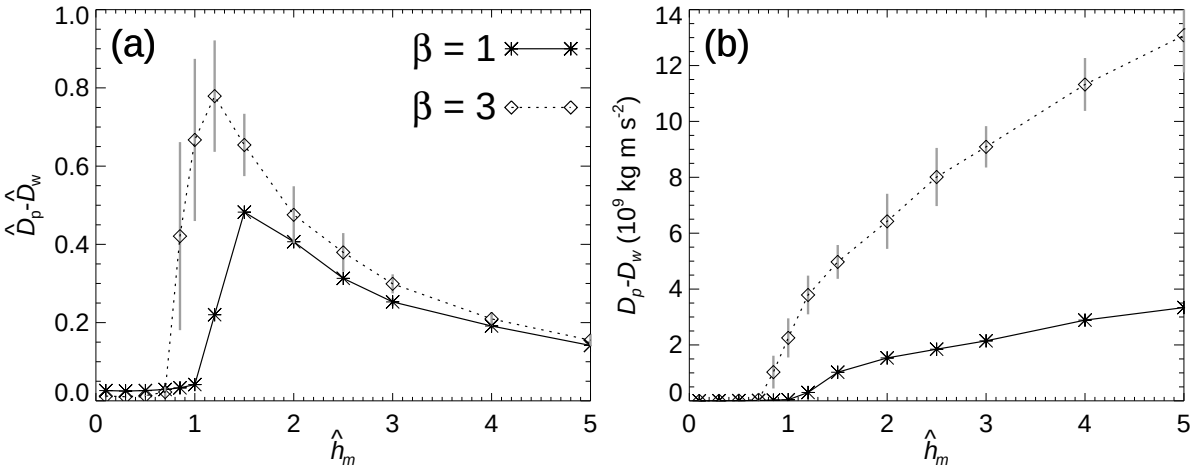

FIG. 17. (a) Normalized and (b) absolute mean flow-blocking drag versus $\hat{h}_m$ for the $\beta = 1$ (solid) and $\beta = 3$ (dotted) obstacles.

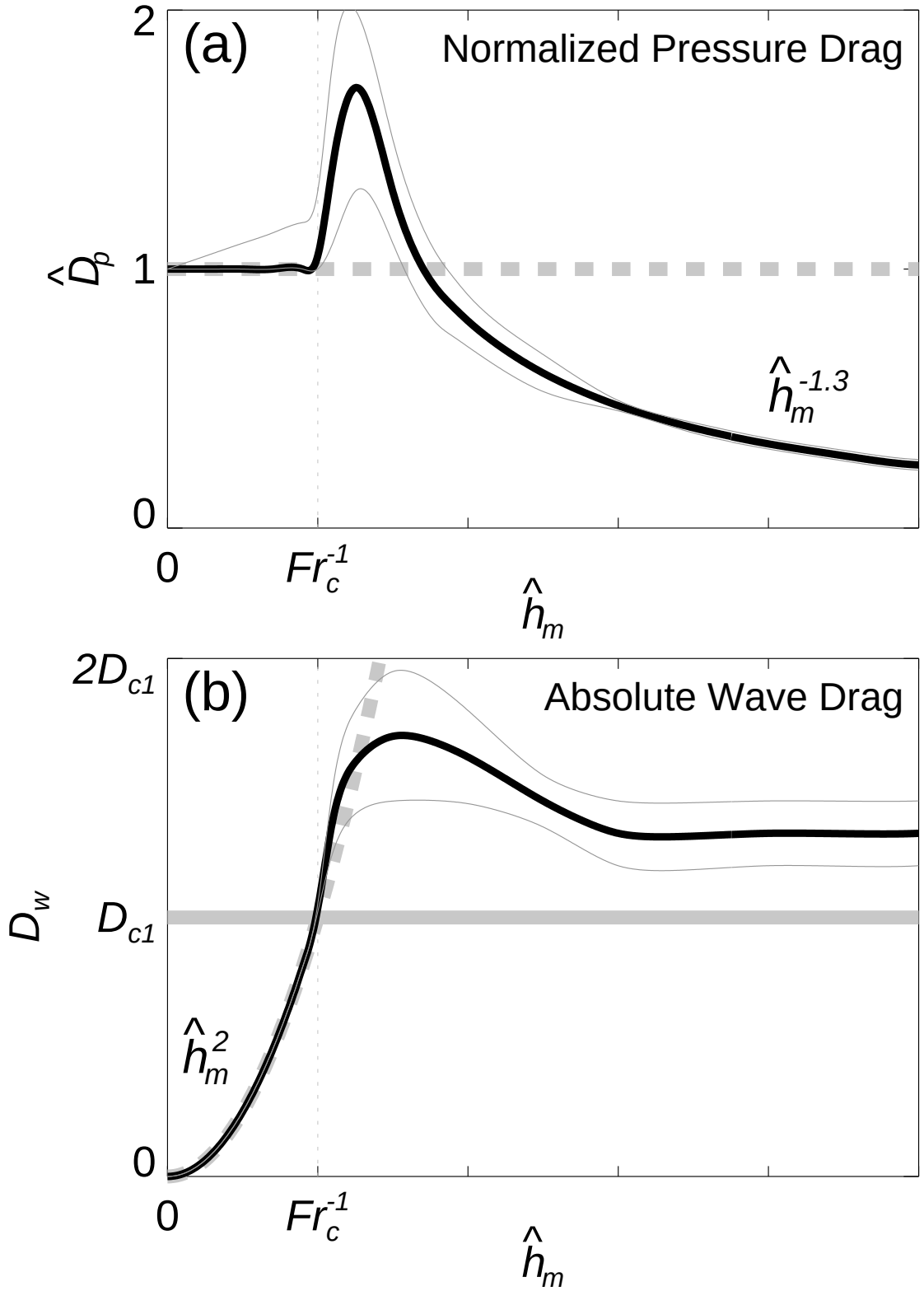

FIG. 18. Schematic diagram of the mean trends (black line) and range of variability (thin gray lines) in (a) nondimensional surface pressure drag $\hat{D}_p$ and (b) absolute wave drag D_w versus $\hat{h}_m$, based on WRF simulations for the $\beta = 1$ and $\beta = 3$ obstacles.